# Heterogeneous mantle effects on the behavior of SmKS waves and outermost core imaging

Authors: Daniel A. Frost[1], Edward J. Garnero[2], Neala Creasy[3], Jonathan Wolf[4], Ebru Bozdağ[5,6], Maureen D. Long[4], Adeolu Aderoju[2], Reynaldo Vite[6]

1. School of Earth, Ocean, and Environment; University of South Carolina

2. School of Earth and Space Exploration; Arizona State University

3. Earth and Environmental Sciences Division, Los Alamos National Lab

4. Department of Earth and Planetary Sciences, Yale University

5. Department of Applied Mathematics and Statistics, Colorado School of Mines

6. Department of Geophysics, Colorado School of Mines





## Abstract

Seismic travel time anomalies of waves that traverse the uppermost 100-200 km of the outer core have been interpreted as evidence of reduced seismic velocities (relative to radial reference models) just below the core-mantle boundary. These studies typically investigate differential travel times of SmKS waves, which propagate as P-waves through the shallowest outer core and reflect from the underside of the core-mantle boundary m times. The use of SmKS and S(m-1)KS differential travel times for core imaging are often assumed to suppress contributions from earthquake location errors and unknown and unmodelled seismic velocity heterogeneity in the mantle. The goal of this study is to understand the extent to which differential SmKS travel times

are, in fact, affected by anomalous mantle structure, potentially including both velocity heterogeneity and anisotropy. Velocity variations affect not only a wave's travel time, but also the path of a wave, which can be observed in deviations of the wave's incoming direction. Since radial velocity variations in the outer core will only minimally affect the wave path, in contrast to other potential effects, measuring the incoming direction of SmKS waves provides an additional diagnostic as to the origin of travel time anomalies. Here we use arrays of seismometers to measure travel time and direction anomalies of SmKS waves that sample the uppermost outer core. We form subarrays of EarthScope's regional Transportable Array stations, thus measuring local variations in travel time and direction. We observe systematic lateral variations in both travel time and incoming wave direction, which cannot be explained by changes to the radial seismic velocity profile of the outer core. Moreover, we find a correlation between incoming wave direction and travel time anomaly, suggesting that observed travel time anomalies may be caused, at least in part, by changes to the wave path and not solely by perturbations in outer core velocity. Modelling of 1-D ray and 3-D wave propagation in global 3-D tomographic models of mantle velocity anomalies match the trend of the observed travel time anomalies. Overall, we demonstrate that observed SmKS travel time anomalies may have a significant contribution from 3-D mantle structure, and not solely from outer core structure.

Key words: core, body waves, seismic arrays, computational seismology, seismic anisotropy

## 1. Introduction

Over the last few decades, seismic imaging studies have devoted attention to mapping the outermost 100s of km of Earth's outer core. This region holds importance for a number of phenomena, including the chemical evolution of the mantle and core, heat transfer from the core to the mantle, and the generation of Earth's geodynamo (Braginsky & Shmidt, 1984; Mound et al., 2019). Differential travel times between SKS waves multiply reflected from the underside of the core-mantle boundary (CMB), called SmKS (where m is the number of outer core segments between the m-1 underside CMB reflections), have dominated outermost core imaging. This is because they possess the shallowest outer core wave bottoming depths of any seismic body wave core phases (Figure 1), and therefore offer the best resolution of the uppermost outer core. SmKS waves propagate as SV, vertically polarized S waves, in the mantle on the source side and convert to P waves as they cross the CMB, before converting back to SV waves in the mantle on the receiver side. Every reflection from the underside of the CMB involves a $\pi/2$ phase shift of the waveform (Choy & Richards, 1975), similar to multiply-reflected S waves at the surface of Earth (SS, SSS, etc.). Higher multiple SmKS waves have particularly strong sensitivity to the velocity structure of the outermost liquid iron core (Figure 2); in contrast, PKP waves turn in the deeper half of the outer core and are thus less sensitive to the outermost core.

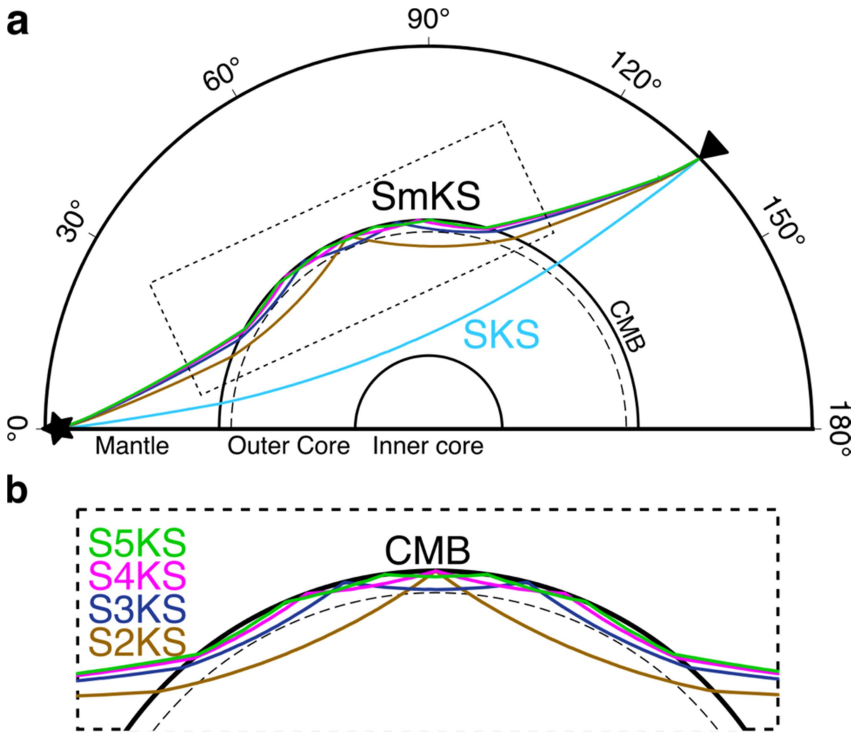


Figure 1. Infinite frequency raypaths of core waves for a source (star) at 200 km depth and receiver (triangle) at 135° distance. **(a)** Higher multiple SmKS paths, where *m* is the number of path segments in the outer core, are most sensitive to the uppermost outer core. The dashed ringed region denotes the outermost 200 km of the outer core below the CMB. **(b)** Expanded section within the dotted box shown in (a) demonstrating that SmKS waves with higher *m* sample the outer core at shallower depths.

Anomalously large timing separations between the travel times of pairs of SmKS waves (i.e., differential travel times) have been interpreted as being due to the more shallowly propagating outermost core wave being delayed relative to the deeper outer core wave (e.g., S4KS is shallower and more delayed than S3KS) compared with predictions from 1-D reference velocity models such as PREM (Adam M. Dziewonski & Anderson, 1981). Reduced P wave speed, Vp, at the top of the core can explain the preferential delays of the relatively shallower outermost

core waves. Thus, most outer core models derived from differential SmKS travel times possess a velocity reduction in the shallowest outermost core relative to background reference models (Figure 2). It is noteworthy, however, that different whole Earth reference models possess significantly different outermost core velocity structures (and importantly, velocity gradients with depth), which also results in differing SmKS differential times. This is important to consider in core modeling, and is often captured in normal mode studies (Irving et al., 2018; Van Tent et al., 2020). Figure 2 shows several such radially averaged models: PREM, iasp91 (Kennett & Engdahl, 1991), AK135 (Kennett et al., 1995), SP6 (Morelli & Dziewonski, 1993), and JB (Jeffreys & Bullen, 1940), and EK137 (Kennett, 2021). We also note some studies have suggested that some SmKS data can be explained without such reductions (Alexandrakis & Eaton, 2010). Past studies of core models shown in Figure 2 are listed in Table 1.

Table 1. Studies with outer core models presented in Figure 2.

| Model name | Study | Whole earth (WE) or outer core (OC) only | SmKS phases "m" | Maximum Vp reduction (%)* | Mantle Corrections? |
|---|---|---|---|---|---|
| JB | (Jeffreys & Bullen, 1940) | WE | Not known | 1.0 | None |
| R71 | (Randall, 1971) | WE | None, direct S only | 0.3 | None |

| | | | | | |
|---|---|---|---|---|---|
| HR71 | (Hales & Roberts, 1971) | WE | 1,2,3 | 2.15 | None |
| SP6 | (Morelli & Dziewonski, 1993) | WE | 1,2 | 1.35 | None |
| AK135 | (Kennett et al., 1995) | WE | 1,2 | 1.35 | None |
| IASP91 | (Kennett & Engdahl, 1991) | WE | 1 | 0.65 | None |
| EPOC-V | (Irving et al., 2018) | WE | (Normal modes) | 0.8 | No |
| EK137 | (Kennett, 2021) | WE | 2,3,4,5 | 0.6 | No |
| KYL | (Young & Lay, 1987) | OC | 1,2 | 1.8 | None |
| KSP | (Souriau & Poupinet, 1991) | OC | 1,2,3 | 10 | None |

| | | | | | |
|---|---|---|---|---|---|
| KGHJ | (Garnero et al., 1993) | OC | 1,2,3,4 | 1.35 | None |
| T15 | (Tang et al., 2015) | OC | 2,3 | 0.24 | None |
| AE09 | (Alexandrakis & Eaton, 2010) | OC | 2,3,4 | 0.1 | None |
| AKbm | (Alexandrakis & Eaton, 2007) | OC | 2,3 | 0.2 | None |
| KT2 | (Tanaka, 2004) | OC | 1,2,3,4 | 1.35 | Yes |
| Tanaka1 | (Tanaka, 2007) | OC | 1,2,3,4 | 1.35 | Yes |
| Tanaka3 | (Tanaka, 2007) | OC | 1,2,3,4 | 0.8 | Yes |
| KOCGA | (Satoshi Kaneshima & Matsuzawa, 2015) | OC | 2,3,4,5 | 0.45 | None |

| | | | | | |
|---|---|---|---|---|---|
| KOCTI | (Satoshi Kaneshima & Matsuzawa, 2015) | OC | 2,3,4,5 | 0.55 | None |
| KHOMC | (S. Kaneshima & Helffrich, 2013) | OC | 2,3,4,5 | 0.45 | None |
| KHOCQ | (Helffrich & Kaneshima, 2010) | OC | 2,3,4,5 | 0.35 | None |
| CCMOC | (Ma & Tkalčić, 2023) | OC | (Coda correlation) | 1 | No |

*Velocities measured relative to PREM

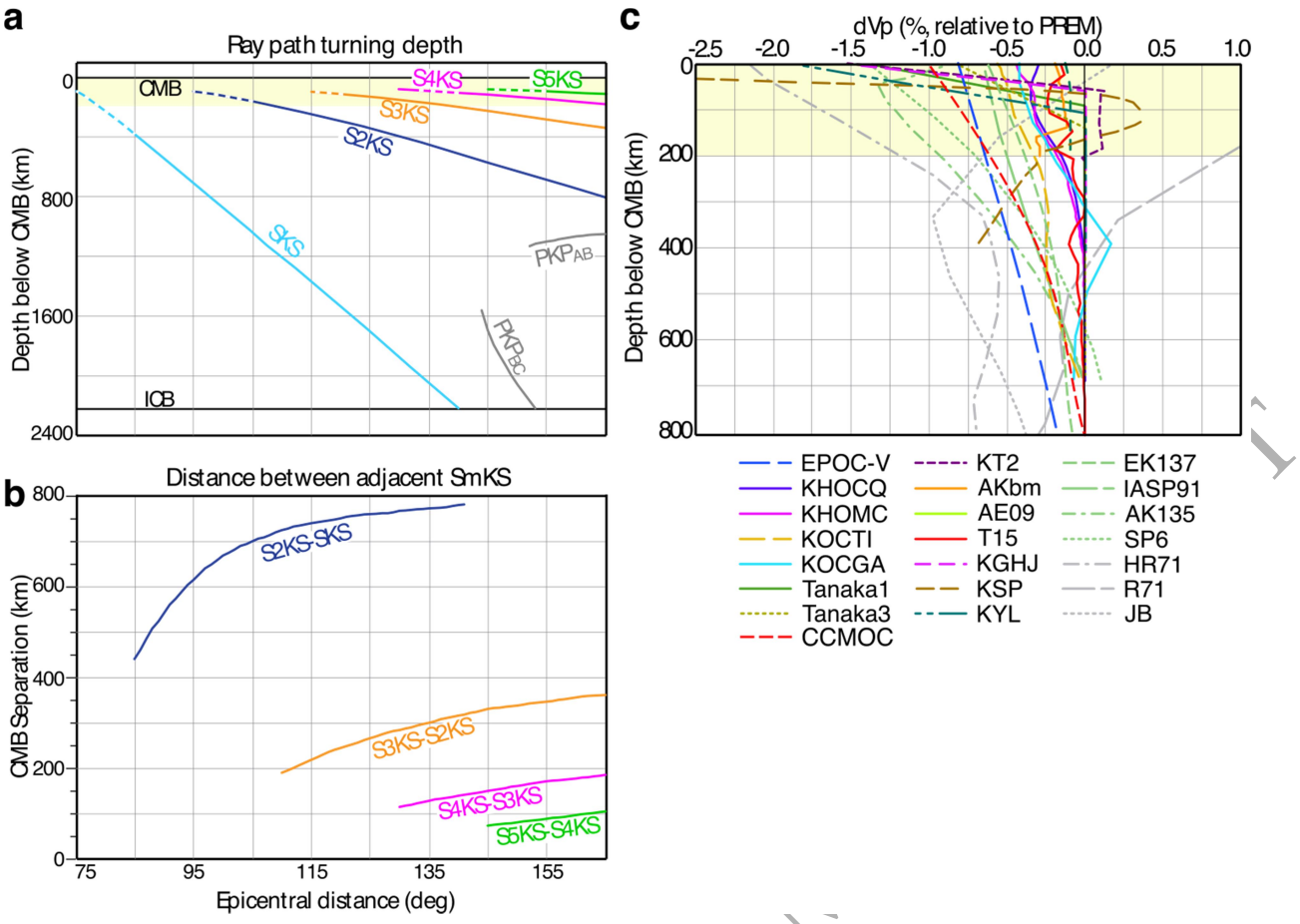


Figure 2. (a) Ray path turning depth estimates for SmKS and PKP waves, using the PREM model. Dashed lines mark where SmKS waves exist but are not typically used due to proximity in time to other contaminating phases and/or are too low in amplitude to observe in single seismograms; however, array methods allow for separation using directivity information. While all core waves traverse the outermost 200 km of the core (shaded), paths of the highest SmKS multiples (e.g., S4KS and S5KS) are solely in this outer shell across all epicentral distances. Similarly, at shorter epicentral distances the lower SmKS multiples (e.g. SKS and S2KS) are also restricted to the outermost core (in contrast to PKP waves which propagate more deeply for all epicentral distances that they are observed. (b) Distance between the CMB piercing points of SmKS differential phase pairs. Higher SmKS multiples show smaller separation distances; thus, the differential time may better minimize the effects of mantle structure. (c) Outermost core Vp

models, shown in percent differences relative to the PREM model (the vertical zero line) for 20 models. The outermost 200 km of the outer core is shaded. Whole earth reference models (IASP91, AK135, SP6, and JB, EK137) and older core models (HR71, R71) show the greatest dissimilarity from PREM, but typically display reduced velocities as well (references to model names are in Table 1).

The relatively close proximity of the adjacent SmKS waves in the deepest mantle, where they enter and exit the core (Figure 1b), has been used to argue that there should be minimal contribution from mantle heterogeneity to SmKS differential times (i.e., lowermost mantle structures should similarly affect adjacent SmKS waves). However, some studies have noted that deep mantle heterogeneity can indeed affect SmKS differential times (Garnero & Helmberger, 1995; Ji & Zhao, 2022; Tanaka, 2014). P and PKP wave branches have also been shown to have sensitivity to both shallow and deep mantle structure (Breger et al., 1999; Durand et al., 2018; Frost et al., 2020; Helffrich & Sacks, 1994; Tkalčić et al., 2002; Ventosa & Romanowicz, 2015; Vidale, 1987). Such effects may be due to heterogeneity at scales smaller than the lateral distance between the pierce points of the different SmKS branches (e.g., 100's of km and less), as well as strong lateral and vertical gradients in lowermost mantle structure, even at large scales (e.g., 1000+ km, laterally). Lateral velocity gradients can perturb a pair of SmKS wave paths, in terms of travel time and also ray parameter and/or back azimuth, each affecting the differential time used for outermost core imaging.

Higher multiple SmKS waves (e.g., S4KS, S5KS, etc.) are best seen at very large distances (e.g., 145° in epicentral distance and greater) (e.g. Helffrich & Kaneshima, 2010). This allows for

sampling of the shallowest outer core, but these phases also have relatively low amplitudes (Figure 3). Seismic array methods that utilize stacking multiple seismograms containing SmKS arrivals can enhance coherent (and otherwise weak) SmKS energy relative to the background noise, allowing analysis of SmKS at larger source-receiver distances and from lower magnitude earthquakes (Eaton & Kendall, 2006; Helffrich & Kaneshima, 2010; S. Kaneshima & Helffrich, 2013; Satoshi Kaneshima & Matsuzawa, 2015; Tanaka, 2004, 2007; Wu & Irving, 2020). Additional information can be obtained using array methods, namely the incoming angle (which is related to seismic wave slowness), and incoming direction (that is, back azimuth). Slowness and back azimuth (here, $u$ and $\theta$, respectively) measurements can be compared to predictions to identify path deviations, if present.

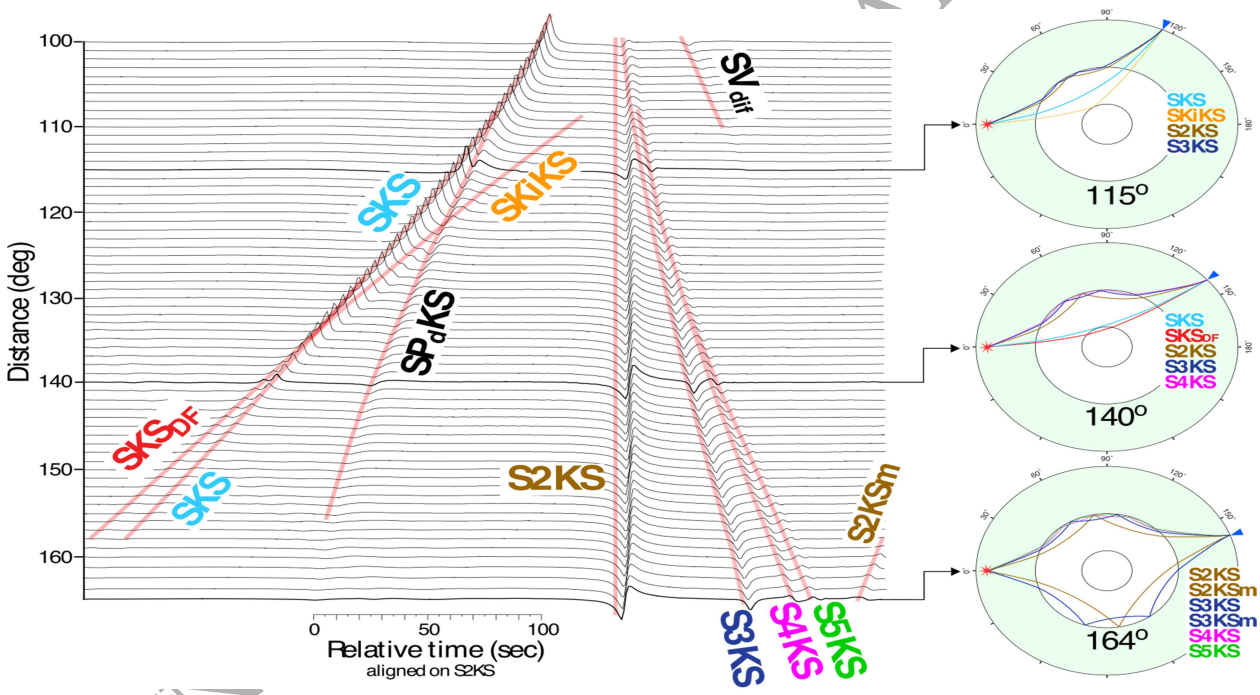


Figure 3. Reflectivity method displacement synthetic seismograms, showing a number of SV core waves. Records are aligned on S2KS. At larger distances, other SV core waves

sensitive to a greater depth range of core structure are present (SkiKS, major arc S2KS, and $SKS_{DF}$). The phase shift of the different SmKS phases is visible. The color of text labels of seismic waves on the left correspond to ray paths in cross-sections on the right.

Variations in the 1-D velocity structure of the outer core would result in travel time and slowness residual anomalies of SmKS waves relative to standard reference model predictions, although the slowness variations would be very small. For example, 1-D outer core model KHOMC (Kaneshima & Helffrich, 2013) reduces the residual travel times of S4KS at 140° by ~3 s relative to PREM, and reduces the residual slowness by_~0.03 s/deg relative to PREM. However, variations in the 1-D velocity structure do not perturb the back-azimuth of a ray. As such, back-azimuth residual anomalies must be due to 3-D velocity perturbations, most likely in the crust or mantle, and large slowness residual anomalies indicate the presence of velocity perturbations in the crust or mantle. Slowness and back-azimuth anomalies signify ray path deviations, which will also perturb the ray path length, and thus will result in travel time perturbations. Therefore, seismic array analyses of slowness and back-azimuth anomalies can be used to investigate the source of differential travel time anomalies of SmKS. Since the outer core is assumed to be nearly laterally homogeneous (Stevenson, 1987), at least at a level detectable seismically, such directional anomalies likely indicate mantle contributions to SmKS travel time and directional anomalies.

The purpose of this work is thus to explore array methodologies to document SmKS slowness, back azimuth, and travel time behaviors, and if anomalies are present, to investigate possible contributions to SmKS differential times from mantle structure, which are often interpreted

solely as being due to outer core structure. In what follows, in section 2, we present an example data set from stations in North America. In section 3, we discuss our data processing methods, including an automated subarray construction process and a beam forming method, which in section 4, we use to determine SmKS timing and wave path direction ($u$, $\theta$) residual anomalies. In section 5, we investigate the influence on SmKS differential times from 3-D mantle heterogeneity using synthetic ray tracing and waveform tools. Lastly, in section 6, we explore other possible contributions from outside of the outer core to documented SmKS anomalies, such as lowermost mantle anisotropy and waveform anomalies (e.g., from crustal structure as well as multi-pathing from seismically sharp deep mantle structures), and discuss the implications of our work for investigations of outermost core structure.

## 2. Data set: basic processing and subarray construction

To investigate array methodologies applied to SmKS waves, we utilize the USArray Transportable Array (TA) from the EarthScope experiment (http://earthscope.org), which has stations spaced closely enough for effective array processing. We selected earthquakes during the time that the USArray was active in the contiguous 48 states (2006-2014) that were at an appropriate range of source-receiver distances for observing SmKS waves (greater than ~100°). Larger distances are required for the highest SmKS multiples to be separated in time (Figure 3). The location and distribution of TA stations and the global distribution of earthquakes during the time period of the EarthScope experiment resulted in no source-receiver distances greater than ~145°. We visually inspected all earthquakes at SmKS distances, and retained data if identifiable SmKS energy (on single seismogram records) was present. Both shallow and deep

focus events were investigated. Table 2 displays the parameters for the 17 retained earthquakes; Figure 4 displays the global map of stations, events, and raypaths.

**Table 1.** Details of the events used in this study. Event parameters are from the Incorporated Research Institutions for Seismology (IRIS). Only events with measurable SmKS waves are shown.

| Event origin time* | Latitude (deg) | Longitude (deg) | Depth (km) | Min/max epicentral distance | # of subarrays used | Phases studied | # of SmKS arrivals measured ** |
|---|---|---|---|---|---|---|---|
| 2006/12/01/ 03:58 | 3.43 | 99.11 | 206.1 | 116.1/131.8 | 137 | SKS, S2KS, S3KS | 323 |
| 2007/04/03 03:35 | 36.52 | 70.69 | 213.0 | 93.9/111.4 | 174 | SKS, S2KS | 315 |
| 2009/09/02 07:55 | -7.73 | 107.41 | 57.8 | 121.3/145.8 | 233 | S2KS | 294 |
| 2009/10/07 21:41 | 4.09 | 122.54 | 586.8 | 102.8/126.7 | 233 | SKS, S2KS, | 499 |

| | | | | | | | |
|---|---|---|---|---|---|---|---|
| | | | | | | S3KS | |
| 2010/07/29 07:31 | 6.56 | 123.36 | 615.8 | 99.8/128.0 | 215 | SKS, S2KS, S3KS | 521 |
| 2011/09/05 17:55 | 3.03 | 98.00 | 106.6 | 117.6/145.6 | 210 | SKS, S2KS, S3KS, S4KS | 528 |
| 2011/12/14 05:04 | -7.53 | 146.81 | 128.5 | 95.1/130.9 | 219 | SKS, S2KS, S3KS | 386 |
| 2012/01/24 00:52 | -24.90 | 178.60 | 579.0 | 83.7/119.7 | 237 | SKS, S2KS, S3KS | 388 |
| 2012/03/21 22:15 | -6.22 | 146.01 | 117.7 | 94.8/130.5 | 257 | SKS, S2KS, S3KS | 569 |

| | | | | | | | |
|---|---|---|---|---|---|---|---|
| 2012/06/23 04:34 | 3.00 | 97.91 | 101.9 | 117.57/149.9 | 259 | SKS, S2KS, S3KS | 660 |
| 2012/08/26 15:05 | 2.20 | 126.87 | 90.9 | 101.4/140.3 | 256 | SKS, S2KS, S3KS, S4KS | 592 |
| 2012/12/10 16:53 | -6.50 | 129.87 | 161.5 | 106.2/144.3 | 242 | SKS, S2KS, S3KS | 342 |
| 2013/04/06 04:42 | -3.47 | 138.47 | 69.4 | 98.1/135.7 | 256 | SKS, S2KS, S3KS | 564 |
| 2013/04/20 04:51 | -6.28 | 130.22 | 113.9 | 105.8/141.5 | 205 | SKS, S2KS, S3KS | 417 |
| 2013/08/12 00:53 | -7.12 | 129.79 | 104.8 | 107.6/143.1 | 150 | SKS, S2KS, S3KS | 216 |
| 2013/09/01 11:52 | -7.54 | 128.26 | 135.5 | 133.3/143.6 | 49 | S2KS | 49 |

| | | | | | | | |
|---|---|---|---|---|---|---|---|
| 2013/09/21 01:39 | -7.27 | 119.95 | 550.1 | 118.4/149.3 | 176 | SKS, S2KS, S3KS | 331 |

* yyyy/mm/dd hh:nn, where: yyyy=year, mm=month, dd=day, hh=hour, nn=minute

** Measurements: slowness and back azimuth deviations relative to PREM, and arrival times

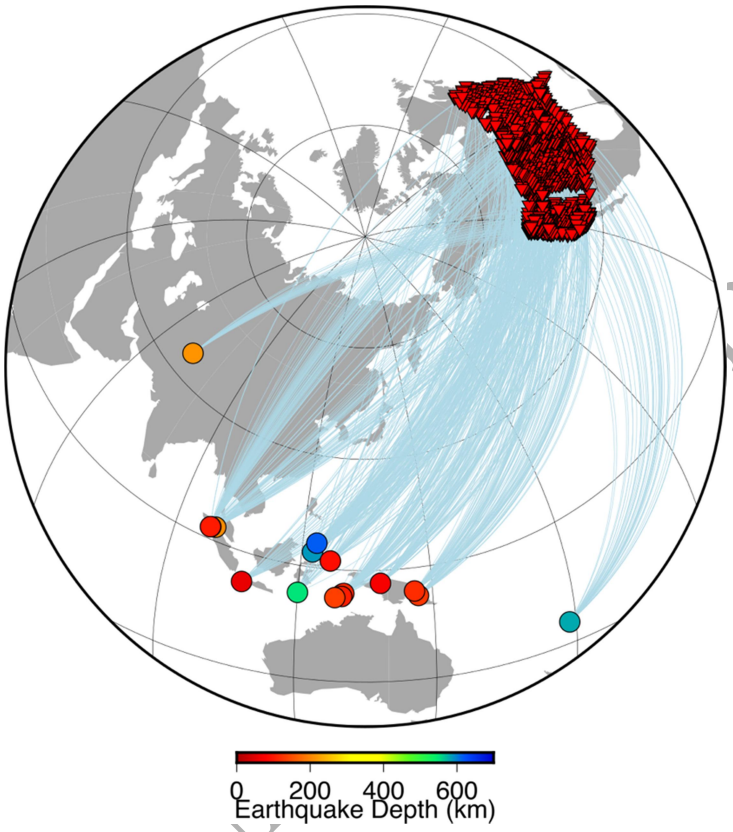


Figure 4. 17 Events (circles, colour coded for earthquake source depth) and stations (red triangles) used in this study. Only stations with measurable SmKS waves are shown. Great circle ray paths between earthquakes and stations are shown as light blue lines.

*2.1 Initial data collection and processing*

For each event in Table 2, three component broadband data were collected, then instrument-deconvolved to displacement, and the horizontal components are rotated to radial (R) and transverse (T) motions relative to the great circle path between events and stations. Data were filtered between 0.02-0.25 Hz. This frequency range proved effective for observing SmKS relative to the background noise in the beam forming process described in Section 3.

*2.2 Subarray construction*

For each event, we construct small geographically localized collections ("subarrays") of USArray stations for subsequent array processing. In a large regional array, such as USArray, subarrays of any geometry, i.e. number of stations, size and shape, can be formed. We determined our preferred array geometry by testing the influence of several geometries on the slowness and back-azimuth resolution of signals arriving from different directions (Figure 5). In this test we hold the number of stations in the array fixed at 15. Using the Direct Solution Method (Kawai et al., 2006), we simulate an S2KS wave using the 1-D PREM model from a 200 km deep event at 120° source-receiver distance, arriving at each array configuration with back-azimuths ranging from 0 to 345° in 15° increments, and measure the apparent slowness and back-azimuth at the array. To determine the ability of each array configuration to accurately resolve signals from different directions, we compare the coherence of the signal (quantified as the F-amplitude, discussed further in Section 3.1), and misfits to the predicted slowness, back-azimuth, and travel time, averaged across all directions. Of the geometries tested, the diamond geometry has both high signal coherence (Figure 5g) and low standard deviation of slowness and

back-azimuth misfit (Figure 5h), demonstrating that this geometry most consistently resolves signals from different directions.

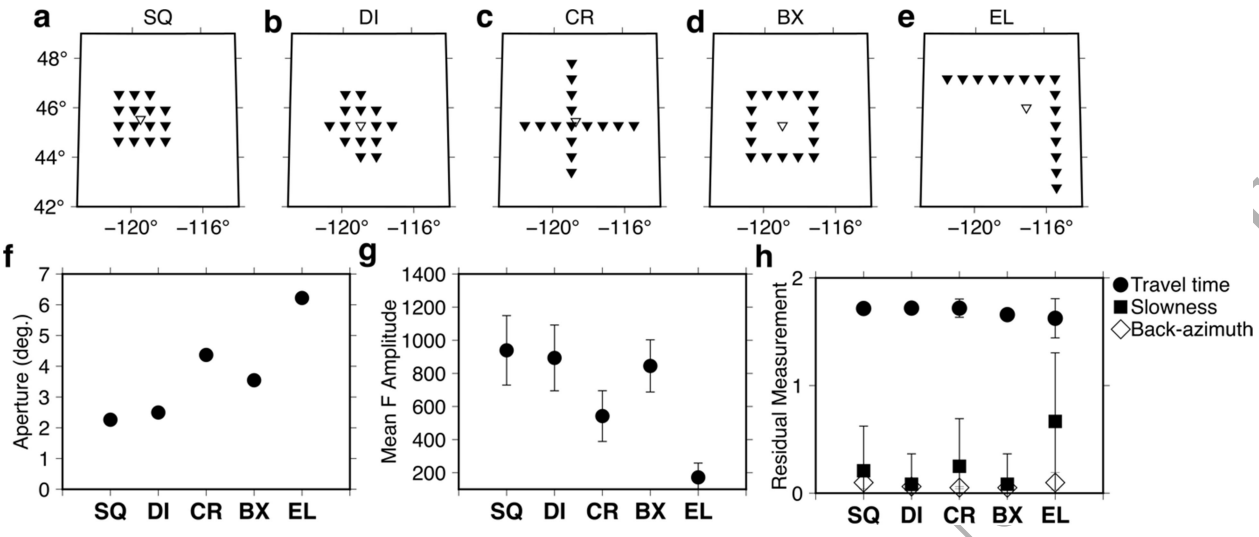


Figure 5. Sensitivities of various subarray geometries. Geometries of stations and the array centre (filled and open triangles, respectively) for (a) Square (SQ), (b) Diamond (DI), (c) Cross (CR), (d) Box (BX), and (e) L-shaped (EL) subarrays. Metrics of each subarray type: (f) maximum aperture, (g) mean F-amplitude, and (h) mean residuals of travel time (black), slowness (square), and back-azimuth (open diamond) in seconds, s/deg, and degree, respectively. Error bars in (f) and (g) show 1 standard deviation from the mean; where errors bars are not visible the measurement errors are smaller than the symbol size.

Subarrays are automatically constructed using the following workflow: (*i*) a 1°×1° grid is defined across the contiguous US for the purpose of potential subarray central positions; (*ii*) for every grid point we determine the closest USArray station; (*iii*) if the closest station is less than 70 km from the grid point, we construct a finer mesh local grid (with 35 km spacing, half the nominal spacing between USArray stations) centered on the previously identified closest (or "central")

station to the 1°×1° grid; (*iv*) within a 280 km wide square, centered on the central station, we identify the closest station to the local, finer mesh grid points (only considering stations up to 70 km away from each of the finer mesh points); (*v*) while prioritizing stations that form a diamond shape with long axes oriented north-south and east-west with 70 km station spacing, we select and retain up to 20 stations from the finer grid. This station selection procedure ensures subarrays with roughly comparable geometries and apertures and thus sensitivities, accounting for the slightly irregular station placements across the USArray. Using a spacing half that of the regular grid (i.e., 35 km) allows us to capitalise on the local increases in station density due to flex-array experiments. This array construction method helps to achieve a relatively fixed array geometry, thus helping to mitigate the need for computing array response functions.

When constructing subarrays, the final number of stations used in each subarray depends on the number of stations proximal to the starting grid point (i.e., from the initial 1°×1° grid). We discard subarrays with fewer than 10 stations; this minimum station number ensures robust slowness and back-azimuth resolution, based on tests with noisy synthetic data. We choose a maximum of 20 stations within the fixed subarray geometry described above. The number of subarrays constructed per event varied between 133 and 265 for our event collection (this depends on how much of the USArray was deployed at the time of each event, as well as viable SmKS distances for each event).

## 3. Beam forming methodology: SmKS slowness, back azimuth, and time measurements

### *3.1 Constructing beam traces from subarray data*

For each successfully constructed subarray, for each SmKS wave that is predicted to arrive at that source-receiver distance (using PREM), we stack the radial component data and produce beams. The location that the beam is considered to represent, called the beam point, of each subarray is set to the arithmetic average location of all stations in the subarray. The beam point is used as a reference location from which to calculate the distance and back-azimuth to the source and to calculate slowness and back azimuth anomalies. Each SmKS phase is stacked separately due to their different slownesses. The Hilbert transformation is applied to SmKS waves (m-1) times (for S2KS and higher multiples) to put each SmKS wave in the same phase as SKS. This allows us to directly compare waveforms (and estimates of residual travel times) between SmKS phases. Data are windowed from 40 s prior to and 40 s after the predicted arrival times of each SmKS wave calculated with the PREM model. This time window may capture multiple SmKS waves, which can be differentiated based on arrival time and slowness. We construct vespagrams by simultaneously grid searching over slownesses from 0 to 9 s/deg in 0.1 s/deg increments, and back-azimuths over a ±20° range in 1° increments relative to the great-circle path, removing the moveout, and stacking the traces to form beams (Davies *et al.*, 1971). We demonstrate this approach with an example even in Indonesia at 3.03°N, 98.00°E and 107 km depth with a magnitude of 6.7 on 2011/09/05 at 17:55 recorded at 14 USArray stations centered in Missouri (Figure 6). Given the size of the subarrays, we use a cylindrically curved wavefront approach (Ward et al., 2020), instead of the typical plane-wave approximation. Next, to suppress aliasing and sharpen the slowness and back-azimuth resolution, we estimate a coherence measurement using the F-statistic ($F$) for each beam (Selby, 2008; Frost et al., 2013). Coherence, $F$, is

computed as the ratio of the sum of the squared energy in the beam, *b(t)*, to the sum of the squared differences between the beam and each trace $x_i(t)$ used to form the beam, in a time window, *M*, normalized by the number of traces in the beam, *N*:

$$F = \frac{(N-1)}{N} \frac{\sum_{t=1}^{M} b(t)^2}{\sum_{i=1}^{N} \sum_{t=1}^{M} (x_i(t) - b(t))^2} \quad (1)$$

Each F-trace is formed from a beam at a specific slowness and back-azimuth. We calculate the F-trace of each beam in our vespagram to form F-trace vespagrams (Figure 6), showing F as a function of time, slowness, and back-azimuth. F-trace vespagrams are visually inspected and we select arrays for which the SmKS wave is well resolved on the F-trace vespagram, and discard those for which the SmKS wave is absent.

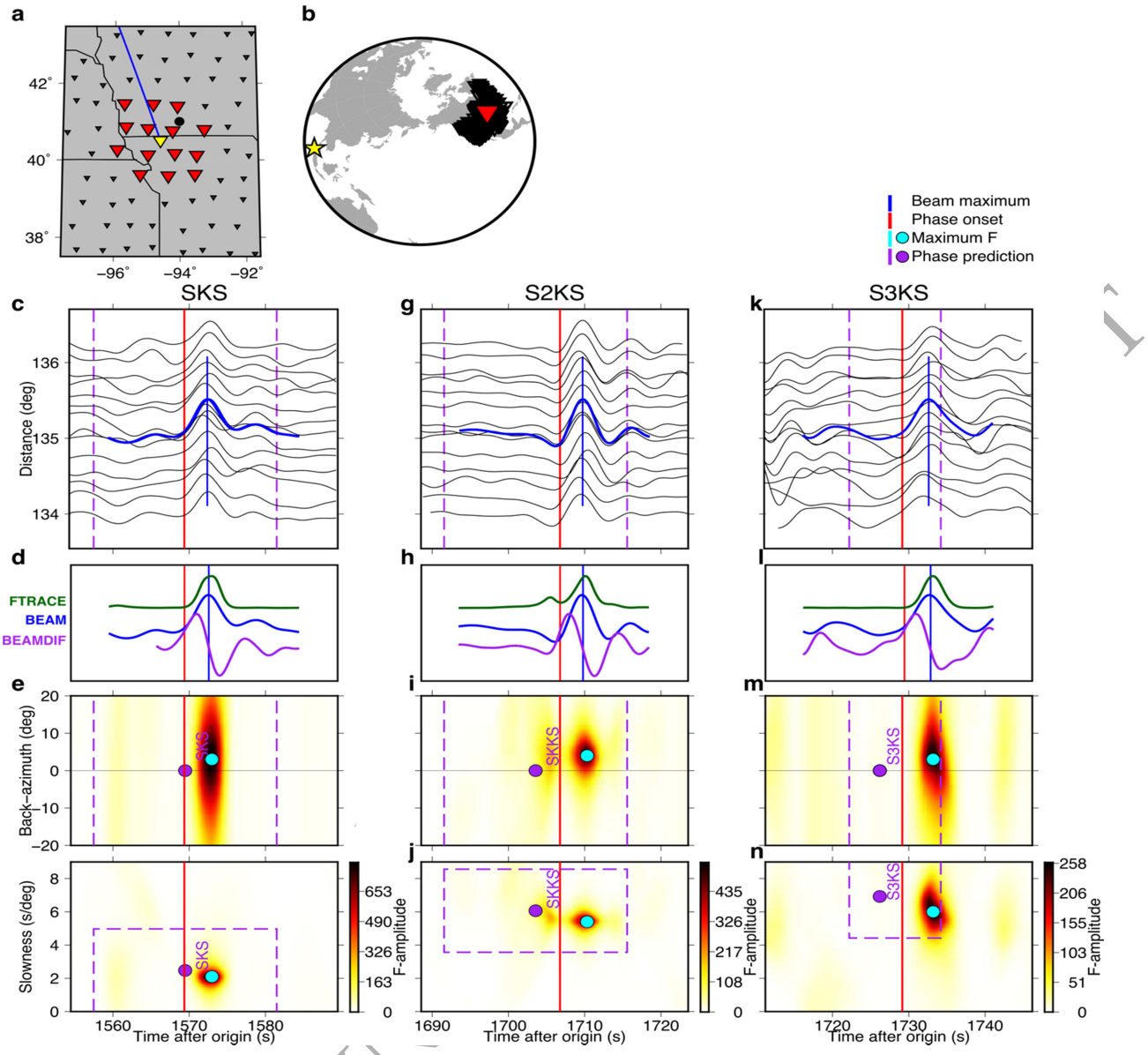


Figure 6. Example F-trace vespagrams for SKS, S2KS, and S3KS phases for a magnitude 6.7 event in Indonesia at 3.03°N, 98.00°E and 107 km depth on 2011/09/05 at 17:55 recorded at 14 USArray stations centered in Missouri. (a) Station map, with red and yellow triangles showing the subarray centre, respectively. Small open black triangles are other USArray stations not used for this subarray. (b) Event (yellow star) and subarray centre (red triangle) locations. The source-receiver distance for this subarray (i.e., at the beam point) is 135°, allowing SKS, S2KS,

and S3KS to be seen clearly, but S4KS is obscured as it arrives only 7 seconds after S3KS. We show radial component traces, normalised to the maximum amplitude across all traces and aligned (c) SKS, (g) S2KS and (k) S3KS. The measured onset, maximum beam amplitude, and pick windows are shown by red, blue, and purple vertical lines, respectively. (d, h, l) Beam (blue), F-trace (green), and differentiated beam traces (purple) and the measured onset (red line) at the solution slowness and back azimuth. F-trace vespagrams in (e, i, m) time back-azimuth and (f, j, n) time slowness space. The maximum F trace amplitude is denoted by a cyan circle. Predicted travel times, slownesses, and back-azimuths are denoted with purple-filled circles, and pick windows are marked by purple lines.

*3.2 SmKS travel time, slowness, and back azimuth measurements*

For every SmKS phase well-resolved in the F-trace vespagrams, we select the slowness and back-azimuth associated with the highest F-trace amplitude. The maximum F amplitude often trails the maximum beam amplitude, since F is a measure of coherence across the individual traces, and small time delays between the maxima in the individual traces reduces this coherence. Instead, we then measure the arrival time of the SmKS wave from the linear beam for that slowness and back-azimuth. To compute SmKS arrival times in an automated fashion, we first extract the maximum beam amplitude in a time window ±12 s around the predicted SKS or S2KS arrival time, and ±8 s around the predicted S3KS or S4KS arrival time (for the polarity predicted from the radiation pattern predictions using focal mechanisms from Global CMT catalogue (Dziewonski et al., 1981; Ekström et al., 2012), and in the phase of SKS). The beam trace is then differentiated to sharpen the onset of the pulse. Then, tracing backwards in time from the maximum of the differentiated beam, we measure the time associated with the

differentiated trace reaching 50% of the maximum amplitude (Zhao et al., 2015). This time is assigned as the arrival time of the phase in the undifferentiated beam trace. The onset times empirically measured using this approach agree well with onsets picked by the naked eye, but with less subjectivity.

Residual SmKS back-azimuths are measured relative to the great-circle path from source to receiver. Travel time and slowness anomalies are measured relative to predictions from PREM, and travel times are corrected for ellipticity (Kennett & Gudmundsson, 1996). In the sub-array example in Figure 6, we measure residual travel times, slownesses and back-azimuths of 4.6 s, 1.0 s/deg, and 9°, respectively, for S2KS, and 4 s, 1.2 s/deg, and 8°, respectively, for S3KS. Uncertainties in these measurements can be approximated from Figure 5, which shows slowness and back-azimuth errors for the diamond and square arrays (roughly equivalent to the array in Figure 6) to be less than 0.1 s/deg and 0.2°, respectively. In real data, additional uncertainties in resolved slowness, back-azimuth, and travel time may result from other sources such as background noise and phase misidentification. We mitigate these through manual inspection of each beam and only select those for which we are confident in the picked parameters.

The beam formed by stacking at the slowness and the back-azimuth with the highest F-amplitude amplifies the signal and suppresses the incoherent noise. We calculate the signal-to-noise ratio (SNR) of each beam's SmKS wave as the ratio between the absolute maximum amplitude of the SmKS phase of interest and the root-mean square of the noise in a time window between 30 and 15 s before that SmKS phase. In the example in Figure 6, the arithmetic average SKS SNR of all

individual unstacked traces is 2.9 with a standard deviation of 4.4. The SKS SNR in the beam increases to 4.6. For the same event, the SNR of S2KS increases nearly three-fold from 9.5 (single trace average, with 1 standard deviation of 4.5) to 24.3 in the beam, and the SNR of S3KS increases from 1.3 (single trace average, with 1 standard deviation of 0.4) to 2.3 in the beam. The increase in the prominence of SmKS phases relative to background noise in beam traces allows more accurate measurements, especially from lower quality events. It also permits measurements from higher multiple SmKS waves that are typically not possible in single seismograms from poorer events, thus allowing for an increased number of SmKS measurements. Moreover, it allows us to observe other low amplitude phases that would otherwise be below the noise level (Supplemental Figure 2).

## 4. Results

### *4.1 Residual anomalies*

For each of the 17 events (Table 2) at each of the subarrays, we measured beam SmKS travel time, T, slowness, u, and back-azimuth, θ, and referenced them to PREM predictions (observed minus PREM) to construct time, slowness and back azimuth residuals (dT, du, dθ, respectively). Systematic geographical variations in these measurements across subarrays are present for each event (Figure 7). Patterns are similar for SKS, S2KS, and S3KS, but with some spatial differences. Residuals are generally smoothly varying with location, particularly for travel time, while slowness and especially back-azimuth exhibits smaller scale spatial fluctuations. Travel time, slowness, and back-azimuth residuals show ranges of -1 to 9 s, -1.24 to 1.47 s/deg, and -20 to 20°, respectively, across all phases, although the majority of the residuals span a smaller range. The observed back-azimuth range is a reflection of the extent of our vespagram grid

search in back azimuth (–20° to +20°). Only a small number of observations lie at the extremes of the back-azimuth range, primarily from some subarrays with poorer data, since back azimuth is the least constrained quantity.

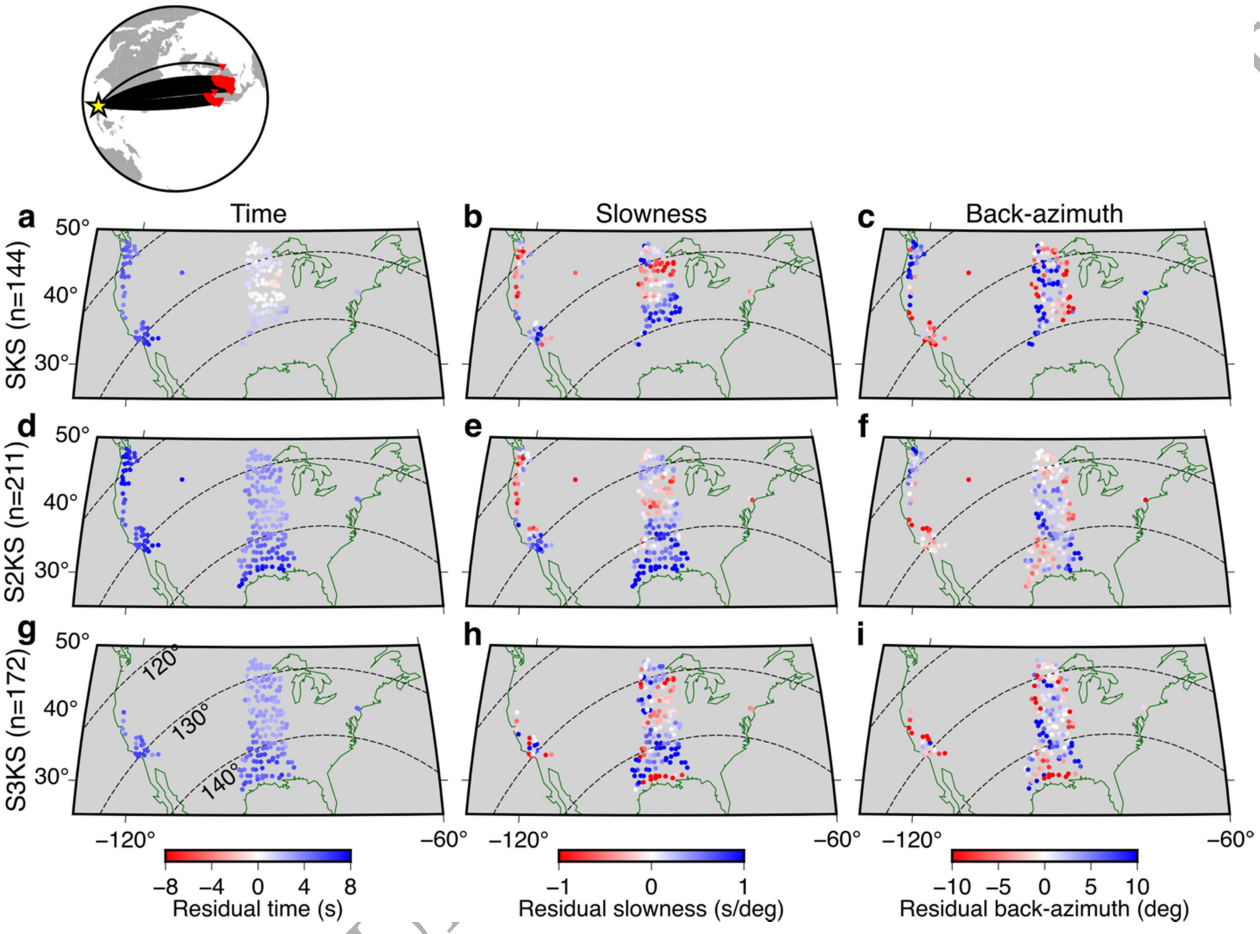


Figure 7. Residual travel time, slowness, and back-azimuth anomalies plotted at subarray location for the event in Indonesia shown in Figure 6 recorded at subarrays across the USArray. Residual travel time, dT, relative to 1-D PREM (first column), slowness, du, relative to 1-D PREM (second column), and back-azimuth, dθ, relative to the great-circle path (third column) anomalies plotted at subarray center locations. Residuals are shown for SKS (top row), S2KS

(middle row), and S3KS (bottom row) with the number of observations, *n*, shown. Residuals for S4KS for this event are not shown due to proximity in time to S3KS. Dashed lines show iso-distances from the source (actual distances plotted in the lower left panel).

Waves with lower slownesses (that is, more vertical raypath direction and more horizontal wavefront) are biased towards larger back-azimuth variability, since back-azimuth goes to infinity for a zero slowness ray (horizontal wavefront). This is particularly important for differential residual measurements between phases of different slownesses, which would have different back-azimuth variabilities. We can remove this uncertainty and make a direct comparison of differences in directional anomalies between the different SmKS branches by transforming residual slowness (du) and back-azimuth (dθ) anomalies to $dU_x$ and $dU_y$, the east-west and north-south components of slowness on the horizontal plane, respectively (Rost and Thomas, 2002).

From the residual anomalies, we calculate differential residual travel time, and $U_x$, and $U_y$ anomalies for each S(m-1)KS and SmKS phase pair, subtracting the phase with lower *m* from the phase with higher *m*, such as SmKS – S(m-1)KS. Since differential residual anomalies can only be calculated at subarrays where both phases are observed, we have fewer differential residual measurements than residual measurements.

Like the residual measurements, the differential residual measurements also show systematic variations in travel time, slowness, and back-azimuth (Figure 8). The spatial patterns vary over several length scales, from 10s of degrees (such as the change from positive to negative

differential travel times from north to south in Figure 8a), to single degrees (such as the rapid variation in $dU_x$ in Figure 8e). Differential travel time, slowness, and back-azimuth residuals show standard deviations of ±1.5 s, ±0.8 s/deg, and ±8°, respectively, across all phases. This demonstrates that the differential measurement does not necessarily cancel traveltime anomalies due to mantle and crustal structure; thus, studies using SmKS differential residuals may attribute some effect of the 3-D Earth crust and mantle to models of the outer core.

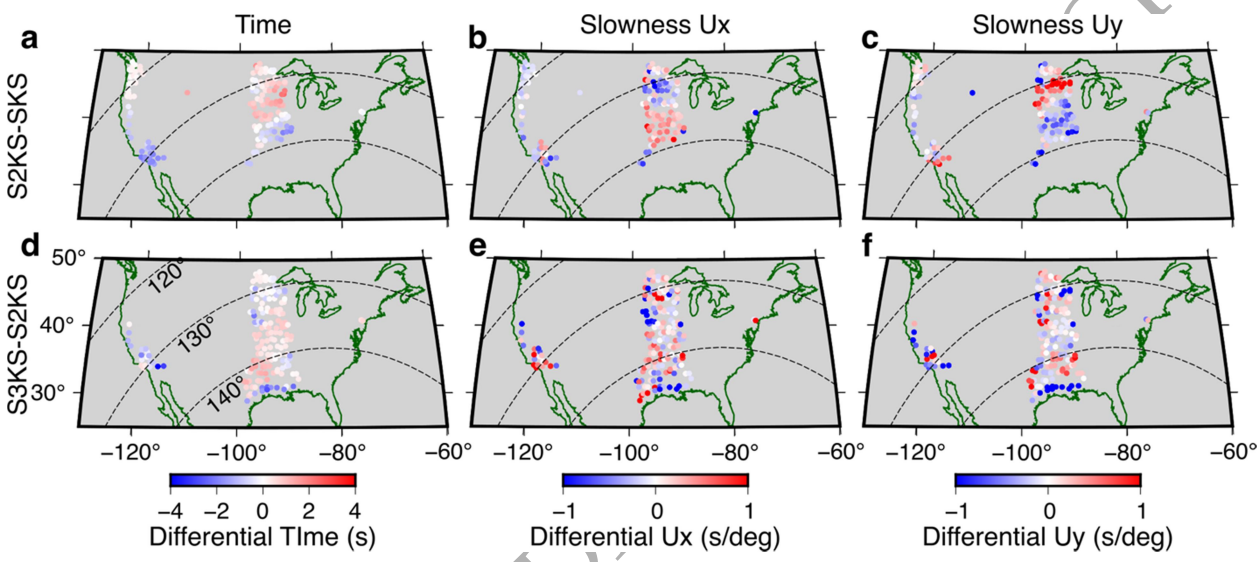


Figure 8. Differential residual travel time, Ux and Uy slowness anomalies plotted at subarray location for the event in Indonesia shown in Figure 6 recorded at subarrays across the USArray. Shown are differentials of (left) travel time, (centre) Ux slowness, and (right) Uy slowness for (top) S2KS-SKS and (bottom) S3KS-S2KS. Dashed lines show iso-distances from the source.

To test our hypothesis that perturbations to the ray path direction either cause, or are an indicator of, travel time anomalies, we compare residual and differential travel times with residual and differential slowness anomalies, dU, for our example event (Figure 9). We find that there is a weak correlation between the magnitude of the residual slowness anomaly and the travel time anomaly, suggesting that perturbations to the ray path do manifest as advancements or delays of the wave. Moreover, this correlation persists for the differential slowness residuals and travel time anomalies, implying that path perturbations are not cancelled by the use of differential travel time measurements. The data shown in Figure 9 are dominantly made at stations in the centre of the U.S. (-100°<longitude<-80°). We find that the residual time versus residual slowness relationship is different for the data recorded at stations on the West Coast of the US (two separate populations for black and cyan points in Figures 9a-c). These two regions have very different crustal and mantle structure in terms of the magnitude, scale, and distribution of velocity heterogeneity, and also great-circle back-azimuths from the event. This may indicate that the effect of mantle heterogeneity on the path may depend on where along the path the heterogeneity is and how the wave interacts with it. However, the differential measurement appears to account for this (with both black and cyan points fitting the same trends in Figures 9d-e). The exact nature of this relationship is the subject of a further ongoing study.

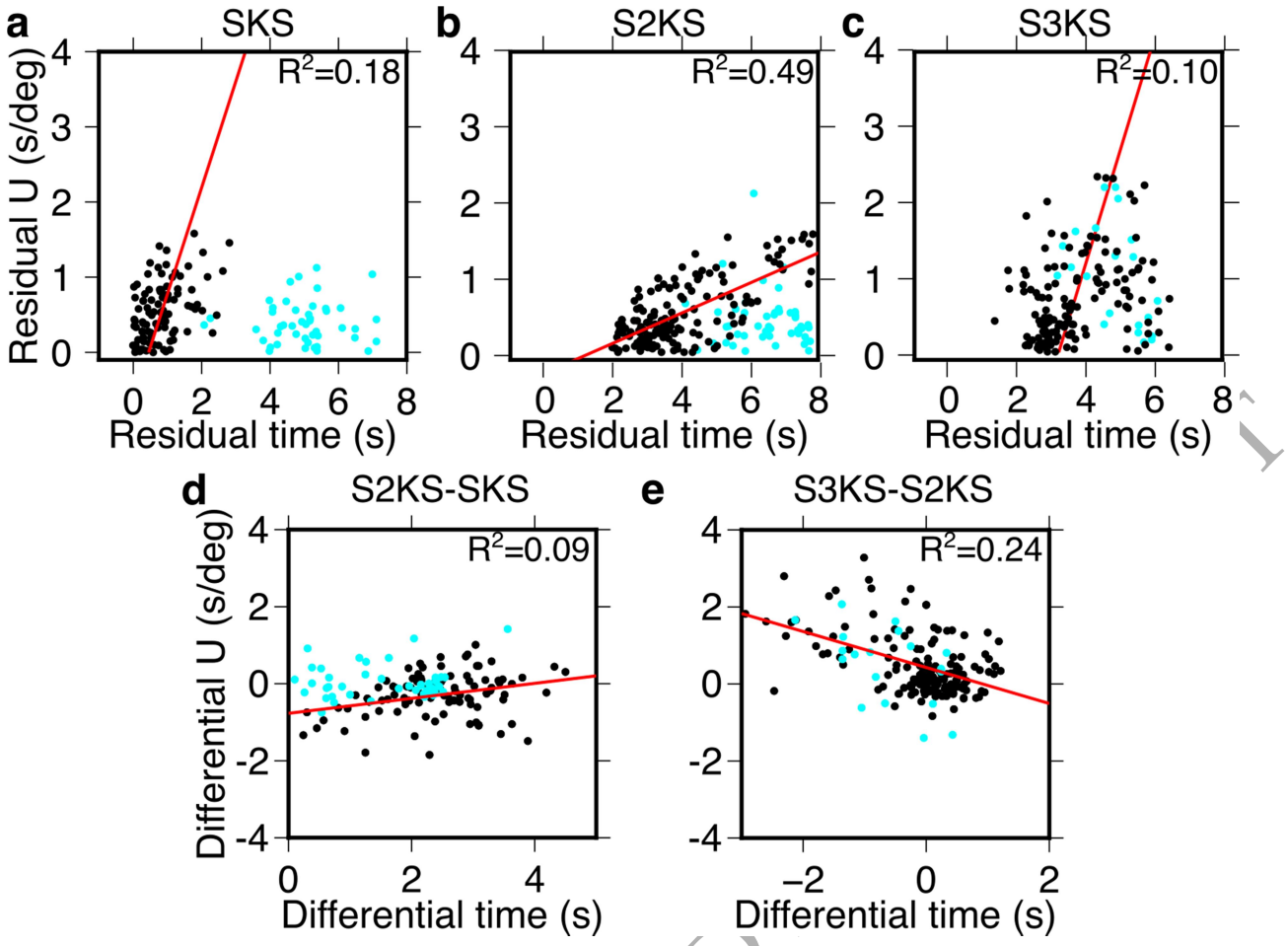


Figure 9. Residual and differential travel time versus slowness anomalies for the event shown in Figure 6. Residual anomalies for (a) SKS, (b) S2KS, and (c) S3KS. Differential anomalies for (d) S2KS-SKS and (e) S3KS-S2KS. Data are fit to a linear regression line, with the $R^2$ fit value shown in the top right corner. Slowness anomalies are converted from slowness and back-azimuth to Ux, Uy, and then the absolute value is taken, prior to calculating the differential. Cyan circles mark observations made at stations on the West Coast of the US (longitudes<-100° in Figure 8); these data are excluded from the regression.

## 5 Estimating heterogeneity effects on SmKS using 1-D and 3-D wave propagation

The paths of SmKS in the mantle and core are perturbed in time and geometry by mantle and crustal heterogeneity. Most past studies of Earth's outer core (Table 1) that have corrected for mantle heterogeneity have utilized 1-D tools, but 3-D effects may be significant on wave propagation. Here we compare travel time anomalies for our example earthquake on 2011/09/05 recorded by the USArray estimated from ray tracing along 1-D ray paths in a 3-D mantle and travel times measured directly from 3-D seismic wavefield simulations computed for 3-D and 1-D mantle models by the 3-D global wave propagation solver SPECFEM3D_GLOBE (Komatitsch & Tromp, 2002a, 2002b).

### *5.1 Estimations of 3-D heterogeneity effects using 1-D tools*

The most commonly used approach to estimate the effects of 3-D mantle heterogeneity on SmKS waves is using 1-D ray tracing in a 1-D reference model (e.g., PREM), and using that ray path to calculate the cumulative effect of velocity perturbations in 3-D mantle heterogeneity models accrued along that 1-D path. The predicted residual travel time anomalies obtained in this way roughly match the pattern and sign of those observed but are generally smaller in magnitude (Figure 10). The mismatch in magnitude may relate in part to tomographic models being damped representations of Earth's actual velocity anomaly amplitudes. Additionally, however, 1-D raytracing through a 3-D tomographic model does not consider perturbation of the wave path itself. As is demonstrated in Figures 7 and 8, there are clear SmKS path perturbations; therefore, accumulating time anomalies along the 1-D ray path is likely insufficient to predict, model, and correct for the true effect of mantle heterogeneities.

As mentioned, the travel time perturbations from a 3-D tomography model can be accrued along the 1-D ray path following the great-circle path. This results in up to several seconds residual time anomaly for any given SmKS. The ray traced residual travel time anomalies approximately match both the spatial distribution (Supplementary Figure 3) and magnitude (Figure 10) of the observed residual time anomalies (Supplementary Figure 3). However, the ray traced differential time anomalies greatly under-predict the magnitude of the observed differential time anomalies (Figure 10d-e). There are two likely reasons for this: (1) because the 1-D ray-paths of the different SmKS phases do not differ significantly, and this method does not account for the ray perturbing effects of 3-D mantle heterogeneity along the exact ray path and finite frequency effects, and (2) because the tomographic models lack the resolution at scales equivalent to the separation between SmKS rays (~100 km laterally). As such, the differential time predictions are not large enough to remove the observed differential time anomalies. Past studies, none of which resolved the slowness and back-azimuth anomalies which are evidence of mantle influence that goes beyond the effect on an approximated 1-D ray, have used travel time residuals in core imaging, despite the possible effects of mantle heterogeneity.

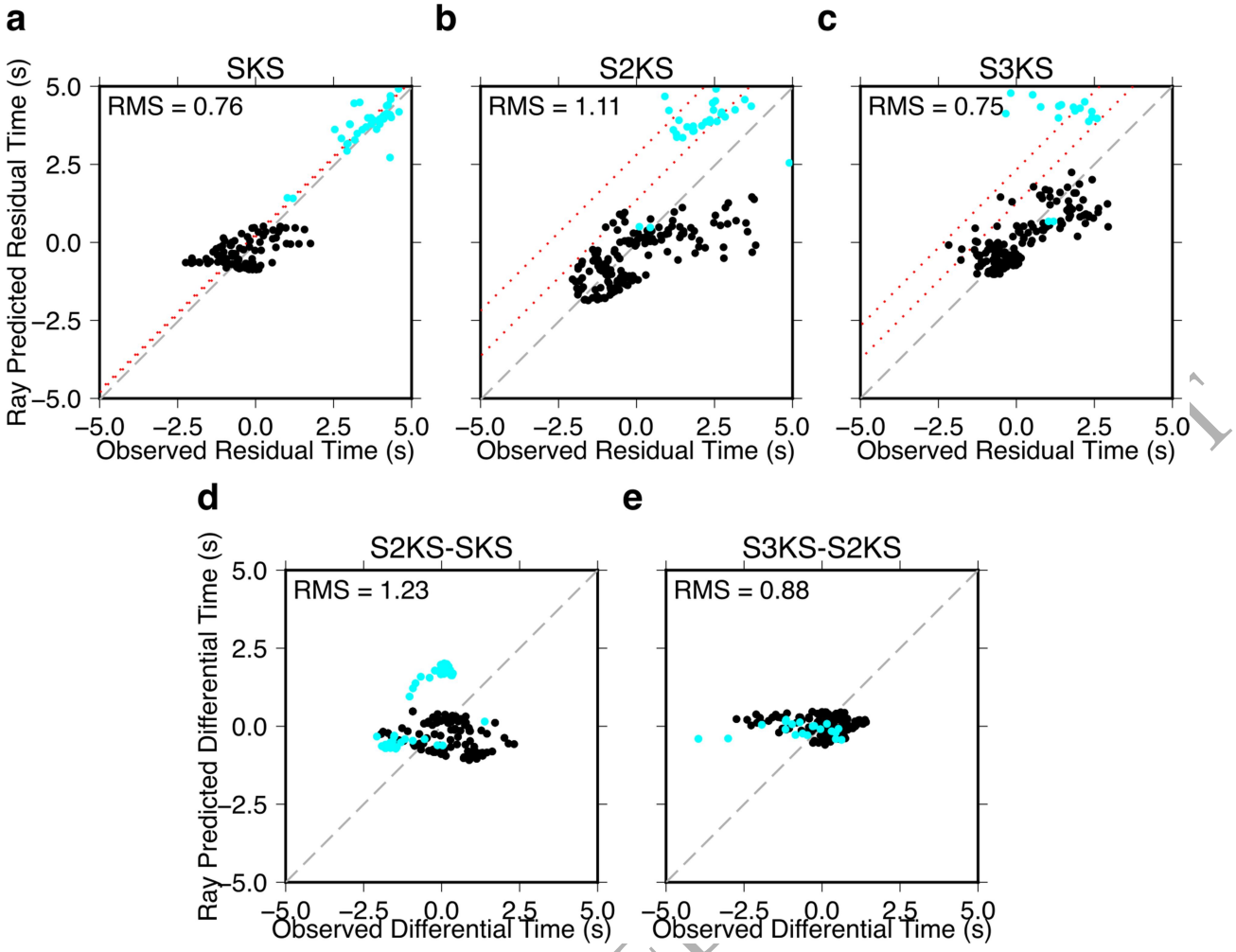


Figure 10. Observed travel times versus travel times anomalies predicted by 1-D raytracing through 3-D models S40RTS for the event shown in Figure 6. Residual travel times for (a) SKS, (b) S2KS, and (c) S3KS and differential travel times for (d) S2KS-SKS and (e) S3KS-S2KS. Synthetic residuals plotted at the receiver location are shown in Supplementary Figure 3. Cyan circles mark observations made at stations on the west coast of the U.S. (longitudes<-100° in Figure 8); these data are excluded from the root mean squared (RMS) misfit calculation shown in the top left corner. Red dotted lines in a-c mark range of residual travel time anomalies predicted from outer core model KHOMC.

*5.2 3-D wave simulations of 3-D heterogeneity effects*

SmKS waves in broadband data typically have dominant frequencies between 0.07 and 0.1 Hz. Thus, finite frequency effects that are not captured by ray theory, which is an infinite frequency approximation (i.e. Marquering et al., 1999), may be important. To assess the effect of mantle structure on waveforms we compute synthetic seismograms and sensitivity kernels for SmKS waves at periods similar to our observed data using the 3-D spectral-element global wave propagation package SPECFEM3D_GLOBE (Komatitsch & Tromp, 2002a, 2002b). We calculate 38-minute long synthetic seismograms. We run simulations using both 1-D PREM and the 3-D global mantle model S40RTS (Ritsema et al., 2011) with 1-D PREM crust.

First, to determine the regions of the mantle and outer core that SmKS waves are sensitive to, we compute finite frequency kernels with the adjoint method (i.e. Tarantola, 1984), shown in Figure 11. We run forward and adjoint simulations (Liu & Tromp, 2008; Tromp et al., 2005) to compute the synthetic seismograms with a resolution up to ~0.11 Hz using 480 spectral elements at the surface along one side of each of six chunks that forms the globe. For computational efficiency, we performed adjoint kernel simulations at a lower resolution than the synthetic forward simulations we performed to make comparisons to observed data down to ~5 s in the next section and filtered the synthetic seismograms and the corresponding adjoint sources between 0.02 and 0.1 Hz to roughly match the frequency content of our observed data. The simulations are run using 1-D PREM and include the ocean load, ellipticity, self-gravity, rotation, and attenuation, and considering the physical dispersion only in adjoint simulations for computational efficiency, which is approximate enough to capture the shape of body-wave kernels (Komatitsch et al., 2016). The sensitivity kernels demonstrate that SmKS waves are sensitive to (thus their

waveform, travel time, slowness and back-azimuth could be perturbed by) structure in large volumes of the mantle, and that these volumes do not completely overlap between different phases meaning that they are likely affected by the mantle differently. This is further evidence that the reliance on the use of differential residual travel times to negate the effect of mantle structure may not represent all mantle effects, and thus may contain errors. It is worth noting that as frequency of the kernels increases, the waves more closely approximate the infinite frequency ray, therefore kernels simulated up to 0.25 Hz (the upper frequency used to filter our data) would have smaller and more distinct sampling volumes than those computed here. While the kernels could also be computed for 3-D models, our motivation here is to illustrate the general scales of the SmKS wave sensitivities in the mantle, so 1-D models are sufficient.

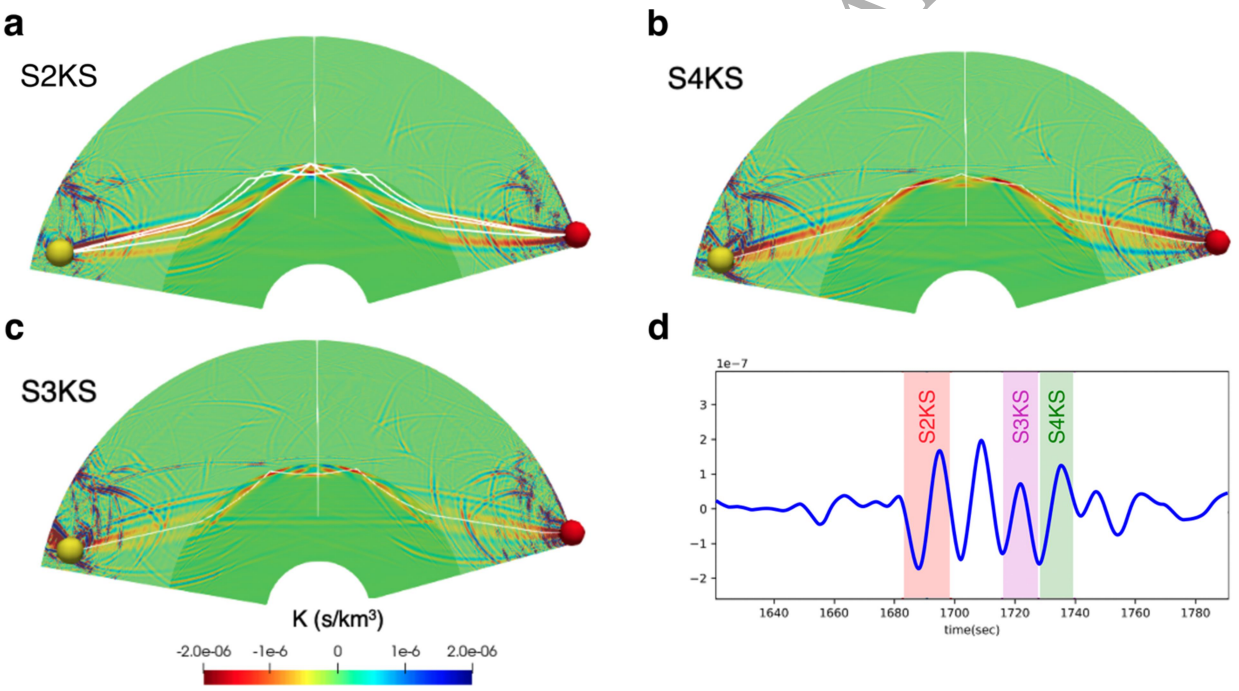


Figure 11. Source–receiver cross sections of the 0.02-0.1 Hz cross-correlation travel time data sensitivity kernels computed by the adjoint method for (**a**) S2KS, (**b**) S3KS, and (**c**) S4KS at a distance of 148° for a 551 km deep event in 1-D model PREM (with no anisotropy). The

sensitivity of each wave to the structure in the mantle and outer core is shown by the colour from red to blue. The infinite frequency ray paths of S2KS, S3KS, and S4KS in a 1-D model are shown by the white lines in **(a)**, and ray paths for S3KS and S4KS are shown faintly in **b** and **c**, respectively. (**d**) Corresponding radial component displacement seismograms with the time windows of each phase for which the kernels are calculated shown as shaded regions.

To measure the effects of 3-D structure on waveforms, we compute synthetic seismograms at 0.2 Hz maximum frequency in the tomography model S40RTS using 768 spectral elements along one side of each of six chunks at the surface. The synthetics are band-passed filtered between 0.02 to 0.25 Hz, exactly like in the data. To ensure similarity between the models used in the 1-D ray tracing and 3-D spectral-element simulations, neither model uses topography, bathymetry, nor ellipticity. The crust is known to be highly laterally heterogeneous, thus most ray-based global tomographic models involve crustal corrections to account for this (e.g. Kustowski et al., 2008; Ritsema et al., 2011). We performed our simulations with the 3-D mantle model S40RTS with the ~24-km thick PREM crust to be consistent with 1-D ray tracing.

We apply our beamforming process to the resulting synthetic seismograms to construct the vespagrams, and measure residual times, $dU_x$, and $dU_y$ for beams computed from synthetics. We reference the measurements from synthetic waveforms computed in S40RTS to synthetic waveforms measured the same way from 1-D isotropic PREM mantle. This avoids any potential bias introduced by referencing a measurement of a synthetic waveform to predictions from ray theory. Residual travel times, $dU_x$ and $dU_y$, for the synthetic seismograms show strong similarity to our observations (Figure 12a-c and Supplementary Figure 4). Furthermore, differential

residual travel times, $dU_x$, and $dU_y$ calculated from the synthetic seismograms show some similarity to the observed data (Supplementary Figure 5). Most importantly, the synthetic differential residual measurements do not cancel the effect of the 3-D structure and the remaining anomalies are of a similar order of magnitude to those observed in the data (Figure 12d-e); unlike the corrections from 1-D ray tracing through a 3-D model (Figure 10d-e), the differentials show systematic variations. This result demonstrates that even for smooth tomographic models and relatively low frequency synthetics (0.02-0.2 Hz), mantle structure can indeed perturb differential SmKS measurements.

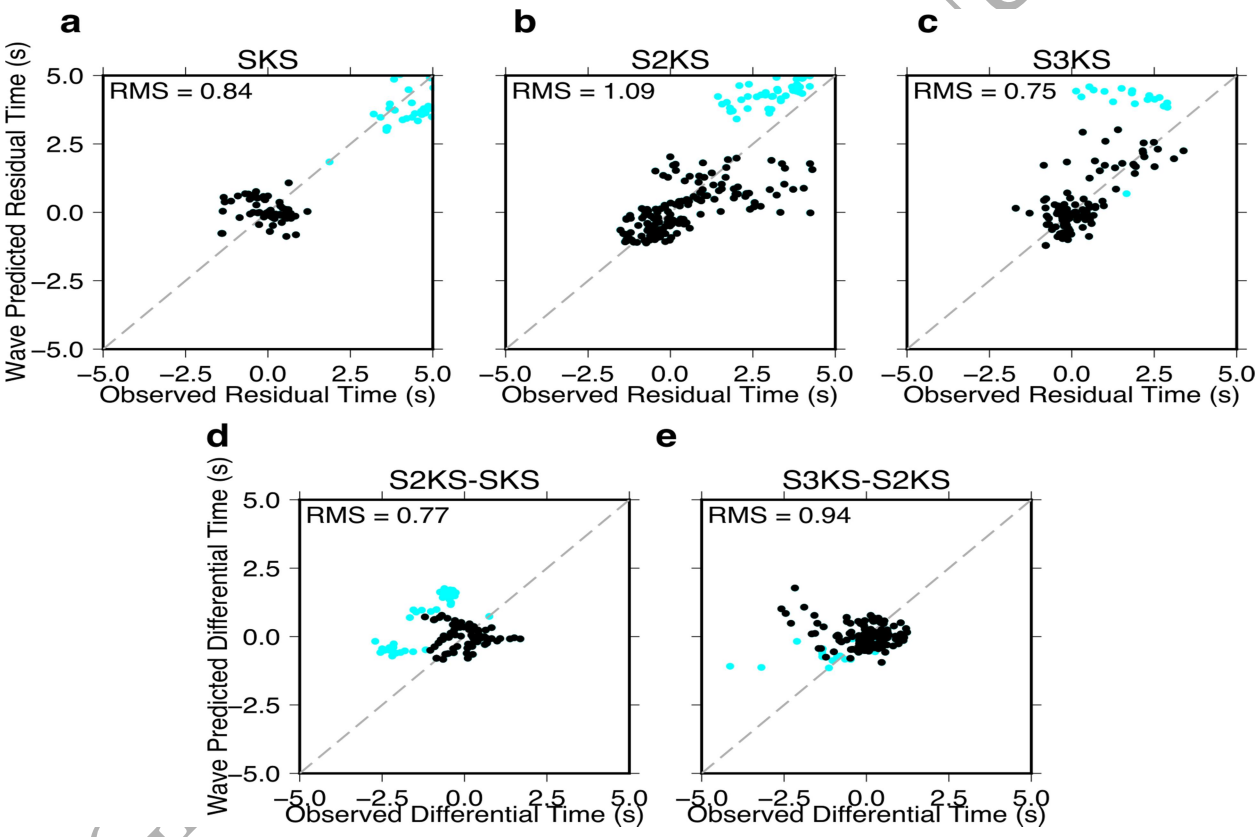


Figure 12. Observed travel times versus travel times anomalies measured from 3-D waveform synthetics calculated for S40RTS (blue) for the event shown in Figure 6. Residual travel times

for (a) SKS, (b) S2KS, and (c) S3KS and differential travel times for (d) S2KS-SKS, and (e) S3KS-S2KS. Synthetic residuals and differentials plotted at the receiver location are shown in Supplementary Figure 4. Cyan circles mark observations made at stations on the west coast of the U.S. (longitudes<-100° in Figure 8); these data are excluded from the root mean squared (RMS) misfit calculation shown in the top left corner.

While our synthetic results generally match the observed data patterns, there are several limitations that may lead to discrepancies. Computing full 3-D waveform synthetics is computationally expensive, so in order to match the frequencies of the data (0.02 to 0.25 Hz) we are limited to fewer synthetic calculations. As such we have only calculated synthetics for our example event and cannot apply this method to all events in the way that the 1-D ray tracing can easily be used. Furthermore, the attenuation structure of the Earth is not well known. This may contribute to small SKS amplitudes at distances >138° and stacking poorly, resulting in no measurements for this phase above this distance. We find that the synthetic waves often have longer codas than the real data, leading to interference between phases. This makes identifying the higher multiples more challenging; as a result, we make no measurements for S3KS at distances less than ~135° due to the longer synthetic wavelength making the phase difficult to separate from S2KS.

Our method of referencing the residuals of the waveform synthetics from the 3-D models to the waveform synthetics from 1-D PREM can help to minimize this challenge, since both models have similar waveform interference. Given that we ignore the heterogeneity in the crust, the synthetic anomalies that we observe are thus the lower limit of what may be. The exploration of

the 3-D crustal effects on SmKS cases is the subject of future work. The spatial resolution in tomographic models is also controlled by other factors related to the inversion, such as damping in linearized inversions. In addition, the frequency of the simulated waveforms controls the scale of the velocity structure that they are sensitive to. Thus, our simulations (at lower frequencies) may be unable to replicate the effects of the smaller spatial scales of structure that the observed SmKS waves (at higher frequencies) are sensitive to. Nonetheless, predictions from 3-D waveform synthetics using 3-D tomographic models will likely best correct for mantle structure, since 3-D effects are accounted for. This maximizes suppression of mantle effects on SmKS, and thus improves sensitivity of SmKS measurements to the outer core.

The similarities between the observed and synthetic residual measurements demonstrates that such patterns are caused by structure in the mantle. More importantly, similarities between the observed differential residual measurements and synthetic differential residual measurements demonstrates both that the mantle can cause these anomalies, and that the differential SmKS measurements likely do not fully cancel the effects of the mantle. However, using 3D waveforms to correct the mantle signal is clearly a better approach compared to 1D ray tracing to address the 3D effects of the chosen mantle model to further improve the outer core structure. The details of the effect of different crustal and mantle models on fits between the observations and predictions will be the subject of future work.

**6. Effect of anisotropy on SmKS differential measurements**

In addition to perturbations of SmKS travel times by 3-D velocity variations in the mantle, it is well-known that seismic anisotropy, the dependence of seismic velocity on wave propagation or polarization direction, in both the upper and lowermost mantle can affect the speed of seismic

waves, including SmKS (e.g. Creasy et al., 2017; Deng et al., 2017; Long et al., 2016; Savage, 1999; Silver & Savage, 1994). Differential SKS-S2KS splitting is usually attributed to lowermost mantle anisotropy because upper mantle raypaths of SKS and S2KS are similar, and both phases therefore essentially sample the same upper mantle anisotropy (Long & Lynner, 2015; Niu & Perez, 2004; Tesoniero et al., 2021; Wolf & Long, 2022). Wolf et al. (2023) demonstrated that the anisotropic signature in beamformed SmKS waves corresponds to an average of the anisotropic contribution to the single-station seismograms that are used to create the beam. Therefore, differences in SmKS and S(m-1)KS beam splitting can be attributed to deep mantle anisotropy in a manner analogous to SKS-S2KS differential splitting measurements; as with SKS-S2KS, the presence of upper mantle anisotropy does not strongly affect differential SmKS-S(m-1)KS travel times. However, differential travel times can potentially be influenced by lowermost mantle anisotropy. For most lowermost mantle regions, seismic anisotropy is only imprecisely characterized, which makes it difficult to explicitly correct for its effects. Therefore, we suggest that studies of isotropic mantle heterogeneity, and studies of outermost core structure, should use SmKS-S(m-1)KS pairs that show nondiscrepant splitting, indicating that the contribution of deep mantle anisotropy is likely weak. Alternatively, such studies could focus on using data that sample the lowermost mantle in regions for which SmKS-S(m-1)KS splitting has been shown to be generally nondiscrepant**.**

## 7. Discussion

We have documented incoming SmKS wavefield direction anomalies across USArray Transportable Array stations using a beamforming approach. The systematic anomalies in residual and differential travel time, slowness, and back-azimuth resolved by our method can

hint at the causative structure. Here we discuss uncertainties with the measurements and the implications of the observations for future work.

*7.1 Measurement Uncertainties*

Due to the array geometry and minimum array size that we choose, the slowness and back-azimuths are well-resolved. For our example event and subarray in Figure 6 (on 2011/09/05 at 17:55), the 90% maximum F-amplitude has a width of ±0.25 s/deg slowness and ±4° back-azimuth for S2KS, and ±0.6 s/deg slowness and ±6° back-azimuth for S3KS.

We estimate the accuracy of our measurement process by measuring travel time, slowness, and back-azimuth for synthetic waveforms calculated using SPECFEM3D_GLOBE for a 1-D PREM velocity structure. We find residual travel time, slowness, and back-azimuth anomalies and standard deviations of ±0.35 s and 0.15s, ±0.2 s/deg and 0.1 s/deg, and ±2° and 0.6°, respectively. These levels of accuracy are considerably smaller than the variations that we observe across the USArray (Figure 7); thus, we conclude that these observed patterns can be attributed to Earth structure and not our beamforming process.

We estimate the sensitivity of the calculated beam to the combination of stations used to form the beam at each subarray by systematically replacing each element of the subarray with another of the nearby stations of the USArray and measuring variation in the measured residual travel time, slowness, and back-azimuth. Resampling our example subarray in Figure 6 thirty times we calculate the standard deviations of the travel time, slowness, and back-azimuth estimates to be 0.1 s, 0.09 s/deg, and 1.2°, respectively, therefore, our observations are robust to changes in the

combination of stations in the subarray. These levels are below the inter-subarray residual travel time, slowness, and back-azimuth differences we observe across the USArray; thus, we conclude that the observed patterns can be attributed to Earth structure.

The subarray geometry that we use was chosen to maximise the robustness and repeatability of the slowness and back-azimuth measurement, while minimising the geographical extent of the subarray, thus allowing us to resolve smaller-scale lateral variations. The subarray method averages the effects of the structure sampled on all rays used to form the beam to a single location, the beam point. To estimate the minimum spatial resolution of our method we calculate the first Fresnel zone radius for a 0.1 Hz SKS wave at 200 km depth beneath the surface and add this to the aperture of an example subarray. We find that the minimum resolution in the upper mantle (200 km depth) is thus approximately 350 km, or 3°, while at the CMB the minimum resolution is ~600 km, or ~10°. Since our sampled regions overlap by about half the width this reduces the sampling width by a factor of 2. Thus we cannot interpret structures smaller than ~200 km in the upper mantle and ~300 km in the lower mantle. Larger array sizes (such as those used in Helffrich & Kaneshima, 2010 and Kaneshima & Matsuzawa, 2015) can be used to increase the signal-to-noise improvement, amplifying weaker phases, but at the cost of decreased spatial resolution. The beamforming method therefore offers the opportunity to systematically study less common SmKS waves, such as major arc phases (e.g., see Supplemental Figure 2).

*7.2 Interpretation of the observed differential measurements*

Across the events that we analyse, we find strong, regional variations in both residual and different travel time, slowness, and back-azimuth anomalies (Figures 13 and 14). While the

observations from different events are sometimes made at the same stations in the USArray, the events will likely sample different parts of the mantle given the different source-receiver azimuths for the different events. As such, we project these measurements to the ray piercing points at CMB. These patterns are robust between different events.

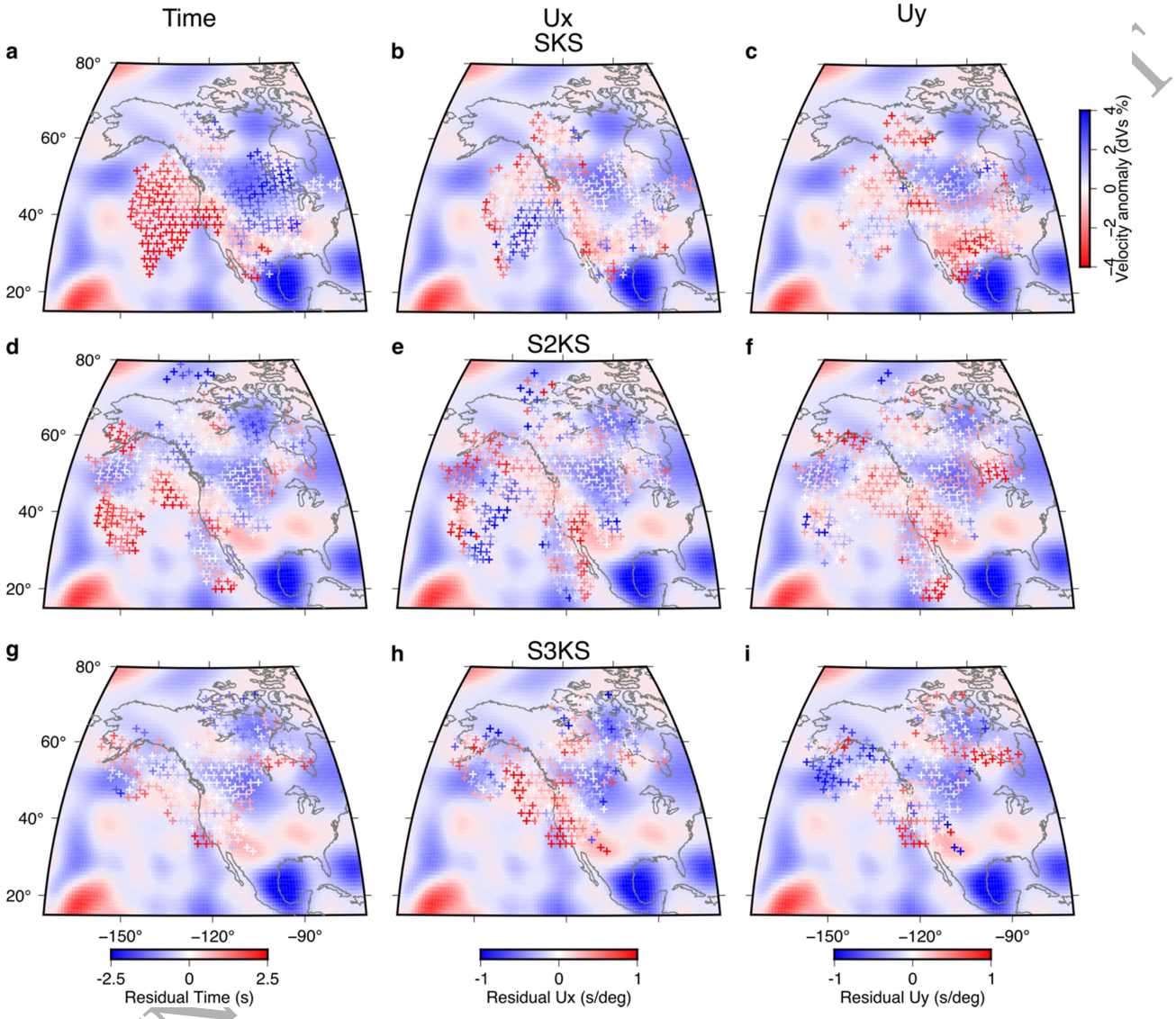


Figure 13. Residual travel time, slowness, and back-azimuth anomalies for all events used in this study, projected to the receiver side core-mantle boundary piercing point and averaged in 2.5° radius gaussian caps. Shown are residuals of travel time (left), slowness (centre), and back-

azimuth (right) for SKS (top), S2KS (middle), and S3KS (bottom). Residuals for S4KS are not shown due lack of adequate measurements. Background is the shear wave velocity anomalies of SEMUCB-WM1 at 2800 km depth. Standard deviations of the average are plotted in Supplementary Figure 6

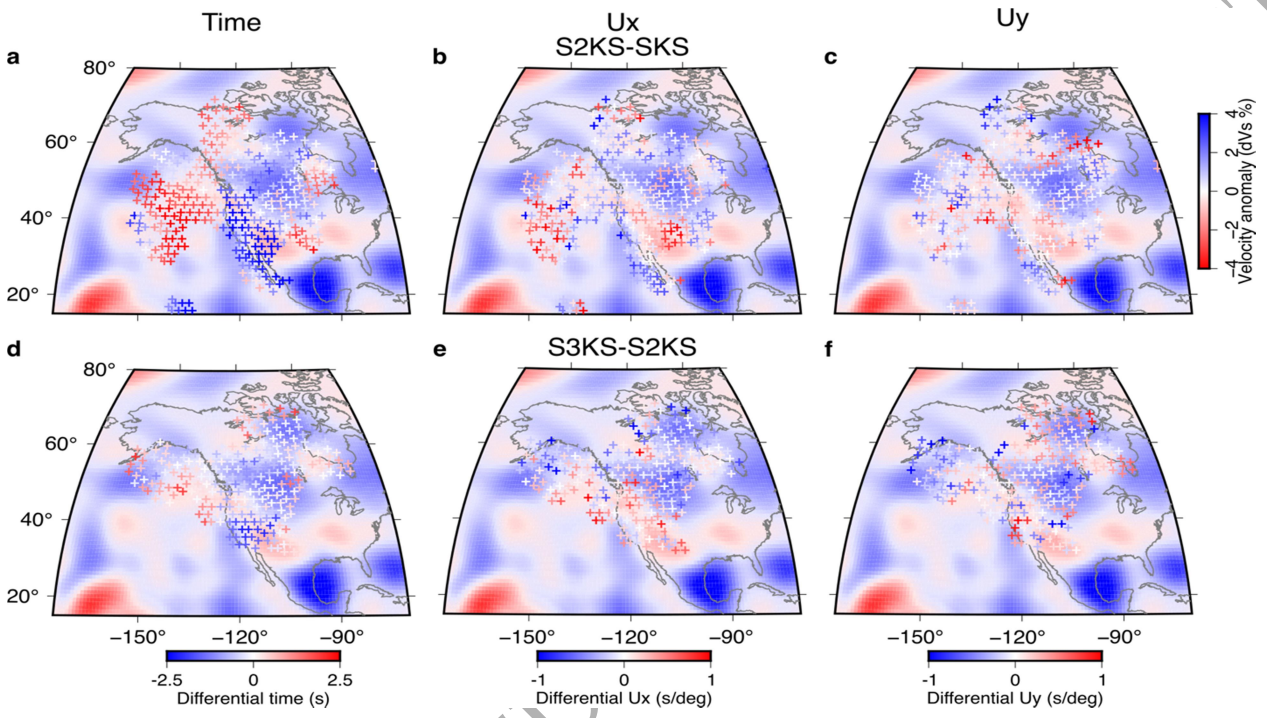


Figure 14. Differential travel time, slowness, and back-azimuth anomalies for all events used in this study, projected to the receiver side core-mantle boundary piercing point and averaged in gaussian caps. Shown are differentials of (left) travel time, (centre) slowness, and (right) back-azimuth for (top) S2KS-SKS and (bottom) S3KS-S2KS. Residuals for S4KS are not shown due lack of adequate measurements. The background is the shear wave velocity anomalies of SEMUCB-WM1 at 2800 km depth. Standard deviations of the average are plotted in Supplementary Figure 7.

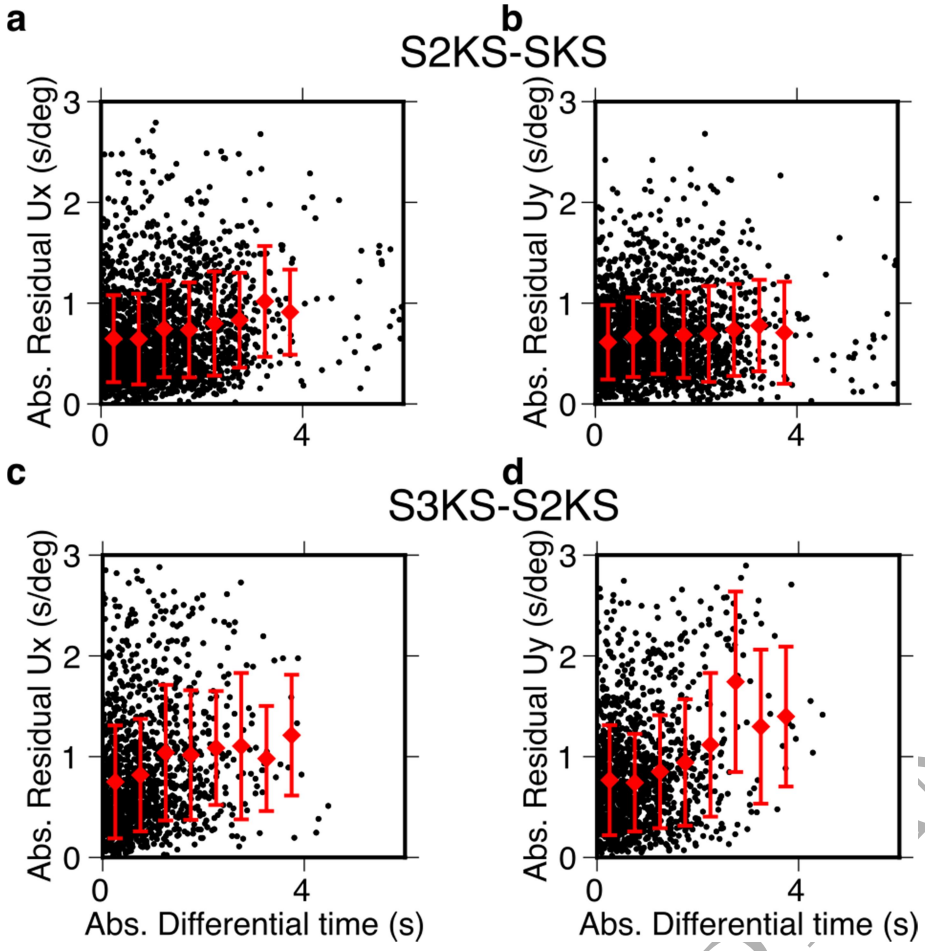


Figure 15. Relationship between absolute differential residual time and maximum residual (a,c) Ux slowness and (b,d) Uy slowness for (a,b) S2KS-SKS and (c,d) S3KS-S2KS for all observations. The maximum residual slowness is the residual of either the first or second phase of the pair that has the greatest magnitude. Averages in 0.5 sec bins are shown as reds symbols, with error bars representing 1 standard deviation.

Previous SmKS studies have interpreted differential travel time anomalies in terms of perturbations to the 1-D radial velocity structure in the outer core, assuming that the differential

calculation sufficiently corrects for mantle and crustal structure. However, our observations of systematically varying differential travel time, slowness, and back-azimuth anomalies, are difficult to reconcile with an outer core origin alone. Ji & Zhao (2022) also demonstrate S3KS-S2KS differential travel time anomalies that vary with back-azimuth and distance. Their synthetic waveform modelling explains a large proportion of the differential travel times that they observed, and they suggest that the remainder may result from the outer core. However, event after applying mantle corrections, travel time anomalies that depend on back-azimuth remain, which is still inconsistent with an outer core cause. A 1-D velocity reduction in the outer core would manifest as a distance-dependent differential travel time anomaly, smoothly increasing with distance. In contrast, we observe distance and back-azimuth dependent travel time anomalies that change on multiple length scales (Figures 8 and 14). Furthermore, while a 1-D velocity reduction relative to PREM in the outer core could result in slowness anomalies relative to PREM, the effect would be significantly smaller than we observe (~0.02 s/deg, which is much less than what we can currently resolve). Moreover, the perturbations to the 1-D radial velocity structure have no effect on the back-azimuth of waves. Instead, we find a systematic relationship between the observed differential travel time anomaly and the observed slowness anomaly (Figure 15), implying that the deviation from the predicted ray direction (which result from mantle structure) can manifest as travel time anomalies.

Other mantle structures on length scales below those resolved in global tomography models could also contribute to differential travel time, slowness, and back-azimuth anomalies. Laterally discontinuous mantle structures could affect a single wave out of a differential wave pair, thus perturbing the differential measurement. For example, Ultra Low Velocity Zones (ULVZs) and

the D″ discontinuity can both be as small as on the order of 100s of km in lateral length scale and are resolved with S-waves of the frequency that we use here (e.g. Garnero & Helmberger, 1996; Whittaker et al., 2016). Furthermore, the Large Low Velocity Provinces (LLVPs) in the lower mantle (e.g. Cottaar & Lekic, 2016; Garnero et al., 2016) are volumes that extend 1000s of km laterally and possibly 100s of km vertically and have reduced seismic velocities. These have been observed to have laterally sharp boundaries between the reduced velocity interior and increased velocity exterior (Ford et al., 2006; Frost & Rost, 2014; Ritsema et al., 1998; To et al., 2005) and sharp lateral contrasts in seismic anisotropy (Ford et al., 2015; Lynner & Long, 2014); these structures may also affect differential SmKS travel time measurements. These structures could be responsible for some of the short wavelength variation in our observed differential measurements (Figures 8 and 16). Given the incompleteness of maps of the smaller scale structure in the lower mantle (e.g Cobden et al., 2015; Yu & Garnero, 2018), we are unable to explicitly correct for these effects.

Variations in lower mantle velocity structure which affect the ray angle may affect the phase shift which occurs as the wave interacts with the CMB. Wang & Niu (2019) found that in some locations the phase shift of some SmKS phases was incomplete, thus following the normal procedure of applying the hilbert transform led to up to 0.6 s differential travel time, which was caused by only by the waveform difference and not a wave propagation speed difference. In our data we do not document whether the waveforms of the different SmKS phases, shifted to match the phase of SKS, differ or not, thus we cannot determine if our differential travel times are affected in this way.

Consequently, and given both the observed dependence of differential travel time anomaly on slowness (Figure 15) and the similarity between the observed travel time, slowness, and back-azimuth anomalies and those observed for synthetic seismograms in a 3-D mantle model, we conclude that the majority of observed SmKS travel time anomalies likely result from mantle and crustal structure that is incompletely cancelled by the differential measurement. Consequently, previously produced models of the velocity structure of the uppermost outer core produced with SmKS observations have likely relied on data sets that have included "contamination" from mantle structure, like that documented here. Models derived from normal modes, such as that of Irving et al. (2018), are likely not contaminated in the same way, although this model does still rely on mantle and crustal corrections. Optimistically, however, measuring the slowness and back-azimuth deviations of SmKS data using an array approach will allow us to identify those measurements with minimal path perturbations (which are therefore minimally influenced by mantle structure), which can then be used for more accurate outer core imaging.

## 8. Conclusions

Differential residual travel times of SmKS waves are commonly used to derive the radial velocity profile in the uppermost outer core. Using small subsets of stations from the USArray, we demonstrate that we can effectively measure a large number of SmKS arrivals by increasing the SNR through stacking and measure the incoming direction of the wave through a vespagram and beamforming approach. We find systematic variations in residual travel time, slowness, and back-azimuth of SmKS values of -1 to 9 s, -1.24 to 1.47 s/deg, and -20 to 20°, respectively, across all studied SmKS phases. Differential residual travel times of SmKS are often assumed to be minimally affected by mantle structure, yet here we demonstrate that differential

measurements still show standard deviation of anomalies of ±1.5 s, ±0.8 s/deg, and ±8° for travel time, slowness, back-azimuth, respectively. These anomalies vary both laterally and with distance, in contrast to predictions from models of radial velocity variations in the uppermost outer core, which would only generate anomalies as a function of distance. We demonstrate that similar patterns of differential residual anomalies can be reproduced by predicting travel times and waveforms through 3-D velocity models of the mantle. These results suggest that SmKS differential measurements, while they suppress some effects of mantle structure, are still significantly affected by the crust and mantle, and thus are not fully representative of radial velocity structure in the outermost core. Furthermore, we suggest that future studies of outermost core structure that rely on SmKS differential travel times should explicitly identify likely contamination by mantle heterogeneity and/or anisotropy, and either apply explicit corrections to account for these effects or focus on subsets of data that appear uncontaminated by mantle effects.

## 9. Acknowledgements

This material is based upon work supported by the National Science Foundation under Award No. EAR-2027181 to D.A.F, EAR-1855206 to N.C., EAR-2026931 to E.B., EAR-2027077 to E.J.G. and A.A, EAR-2026917 to M.L. and J.W.

The Los Alamos National Laboratory (LANL) access is available through LA-UR 23-29864.

We thank the Earthscope experiment, USArray, and the Incorporated Research Institution for Seismology (https://www.earthscope.org/; http://www.usarray.org/; https://www.iris.edu/hq/) for

the open access to all the data used in this study. CMT solutions come from the Global CMT project (https://www.globalcmt.org/). The open source spectral-element software package SPECFEM3D_GLOBE is freely available via Computational Infrastructure for Geodynamics (CIG, https://geodynamics.org/resources/specfem3d).

**Author Contribution Statement**

D.A.F and E.J.G. were responsible for the conceptualisation of the work. D.A.F, E.J.G, M.D.L., and E.B. were responsible for funding acquisition and supervision. E.J.G. was responsible for data acquisition. D.A.F., E.B., and N.C. were responsible for the methodology, software, and visualisation. All authors took part in discussion of the results and in writing and editing.

**Data Availability Statement**

Data from the TA network were made freely available as part of the EarthScope USArray facility, operated by Incorporated Research Institutions for Seismology (IRIS) and supported by the National Science Foundation, under Cooperative Agreements EAR-1261681.

**10. References**

Alexandrakis, C., & Eaton, D. W. (2007). Empirical transfer functions: Application to determination of outermost core velocity structure using SmKS phases. *Geophys. Res. Lett.*, *34*(22), 1–5. https://doi.org/10.1029/2007GL031932

Alexandrakis, C., & Eaton, D. W. (2010). Precise seismic-wave velocity atop Earth's core: No evidence for outer-core stratification. *Phys.*, *180*(1–2), 59–65. https://doi.org/10.1016/j.pepi.2010.02.011

Braginsky, S. I., & Shmidt, O. Y. (1984). Short-Period Geomagnetic Secular Variation. *Geophysical & Astrophysical Fluid Dynamics*, *30*(1–2), 1–78. https://doi.org/10.1080/03091928408210077

Breger, L., Romanwicz, B., & Tkalčić, H. (1999). PKP(BC-DF) travel time residuals and short scale heterogeneity in the deep earth. *Geophys. Res. Lett.*, *26*(20), 3169–3172.

Choy, G. L., & Richards, P. G. (1975). Pulse distortion and Hilbert transformation in multiply reflected and refracted body waves. *Bull. Seism. Soc. Am.*, *65*(1), 55–70. Retrieved from http://bssa.geoscienceworld.org/content/65/1/55%5Cnhttp://bssa.geoscienceworld.org/content/65/1/55.full.pdf

Cobden, L., Thomas, C., & Trampert, J. (2015). Seismic detection of post-perovskite inside the earth. *The Earth's Heterogeneous Mantle: A Geophysical, Geodynamical, and Geochemical Perspective*, *2*, 391–440. https://doi.org/10.1007/978-3-319-15627-9_13

Cottaar, S., & Lekic, V. (2016). Morphology of seismically slow lower-mantle structures. *Geophys. J. Int.*, *207*(2), 1122–1136. https://doi.org/10.1093/gji/ggw324

Creasy, N., Long, M. D., & Ford, H. A. (2017). Deformation in the lowermost mantle beneath Australia from observations and models of seismic anisotropy. *Journal of Geophysical Research: Solid Earth*, *122*(7), 5243–5267. https://doi.org/10.1002/2016JB013901

Davies, D., Kelly, E. J., & Filson, J. R. (1971). Vespa Process for Analysis of Seismic Signals. *Nat. Phys. Sci.*, *232*, 8–13. https://doi.org/10.1038/physci232008a0

Deng, J., Long, M. D., Creasy, N., Wagner, L., Beck, S., Zandt, G., et al. (2017). Lowermost mantle anisotropy near the eastern edge of the Pacific LLSVP: Constraints from SKS-SKKS splitting intensity measurements. *Geophysical Journal International*, *210*(2), 774–786. https://doi.org/10.1093/gji/ggx190

Durand, S., Thomas, C., & Jackson, J. M. (2018). Constraints on D″ beneath the North Atlantic region from P and S traveltimes and amplitudes. *Geophys. J. Int.*, *216*(2), 1132–1144. https://doi.org/10.1093/gji/ggy476

Dziewonski, A. M., Chou, T. A., & Woodhouse, J. H. (1981). Determination of earthquake source parameters from waveform data for studies of global and regional seismicity. *Journal of Geophysical Research*, *86*(B4), 2825–2852. https://doi.org/10.1029/JB086iB04p02825

Dziewonski, Adam M., & Anderson, D. L. (1981). Preliminary reference Earth model. *Phys.*, *25*(4), 297–356. https://doi.org/10.1016/0031-9201(81)90046-7

Eaton, D. W., & Kendall, J. M. (2006). Improving seismic resolution of outermost core structure by multichannel analysis and deconvolution of broadband SmKS phases. *Phys. Earth Planet. Int.*, *155*(1–2), 104–119. https://doi.org/10.1016/j.pepi.2005.10.007

Ekström, G., Nettles, M., & Dziewoński, A. M. (2012). The global CMT project 2004-2010: Centroid-moment tensors for 13,017 earthquakes. *Physics of the Earth and Planetary Interiors*, *200–201*, 1–9. https://doi.org/10.1016/j.pepi.2012.04.002

Ford, H. A., Long, M. D., He, X., & Lynner, C. (2015). Lowermost mantle flow at the eastern edge of the African Large Low Shear Velocity Province. *Earth Planet. Sci. Lett.*, *420*, 12–22. https://doi.org/10.1016/j.epsl.2015.03.029

Ford, S. R., Garnero, E. J., & McNamara, A. K. (2006). A strong lateral shear velocity gradient and anisotropy heterogeneity in the lowermost mantle beneath the southern Pacific. *J. Geophys. Res.*, *111*(3), 1–14. https://doi.org/10.1029/2004JB003574

Frost, D.A., & Rost, S. (2014). The P-wave boundary of the Large-Low Shear Velocity Province beneath the Pacific. *Earth Planet. Sci. Lett.*, *403*. https://doi.org/10.1016/j.epsl.2014.06.046

Frost, D.A., Rost, S., Selby, N. D., & Stuart, G. W. (2013). Detection of a tall ridge at the core-mantle boundary from scattered PKP energy. *Geophys. J. Int.*, *195*(1). https://doi.org/10.1093/gji/ggt242

Frost, Daniel A, Romanowicz, B., & Roecker, S. (2020). Upper mantle slab under Alaska : contribution to anomalous core-phase observations on south-Sandwich to Alaska paths. *Physics of the Earth and Planetary Interiors*, *299*(January), 106427. https://doi.org/10.1016/j.pepi.2020.106427

Garnero, E. J., & Helmberger, D. V. (1995). On seismic resolution of lateral heterogeneity in the Earth's outermost core. *Phys. Earth Planet. Int.*, *88*(2), 117–130. https://doi.org/10.1016/0031-9201(94)02976-I

Garnero, E. J., & Helmberger, D. V. (1996). Seismic detection of a thin laterally varying boundary layer at the base of the mantle. *Geophys. Res. Lett.*, *23*(9), 977–980.

Garnero, E. J., Helmberger, D. V., & Grand, S. P. (1993). Constraining outermost core velocity with SmKS waves. *Geophys. Res. Lett.*, *20*(22), 2463–2466. https://doi.org/10.1029/93GL02823

Garnero, E. J., McNamara, A. K., & Shim, S.-H. (2016). Continent-sized anomalous zones with low seismic velocity at the base of Earth's mantle SUPPLEMENTARY. *Nature Geosci.*, 1–14. https://doi.org/10.1038/NGEO2733

Hales, A. L., & Roberts, J. (1971). Velocities in outer core. *Bull. Seism. Soc. Am.*, *61*(4), 1051.

Helffrich, G., & Kaneshima, S. (2010). Outer-core compositional stratification from observed core wave speed profiles. *Nature*, *468*(7325), 807–812. https://doi.org/10.1038/nature09636

Helffrich, G., & Sacks, S. (1994). Scatter and bias in differential PKP travel times and implications for mantle and core phenomena. *Geophys. Res. Lett.*, *21*(19), 2167–2170.

https://doi.org/10.1029/94GL01876

Irving, J. C. E., Cottaar, S., & Lekic, V. (2018). Seismically determined elastic parameters for Earth's outer core. *Science Advances*, *4*(6), 1–10. https://doi.org/10.1126/sciadv.aar2538

Jeffreys, H., & Bullen, K. E. (1940). Seismological Tables. *British Association for the Advancement of Science, London*.

Ji, Q., & Zhao, L. (2022). Automatic measurement and quality control of S3KS-SKKS differential traveltimes and the influence of mantle heterogeneity. *Geophysical Journal International*, *229*(2), 1448–1461. https://doi.org/10.1093/gji/ggac001

Kaneshima, S., & Helffrich, G. (2013). Vp structure of the outermost core derived from analysing large-scale array data of SmKS waves. *Geophys. J. Int.*, *193*(3), 1537–1555. https://doi.org/10.1093/gji/ggt042

Kaneshima, Satoshi, & Helffrich, G. (2013). Vp structure of the outermost core derived from analysing large-scale array data of SmKS waves. *Geophys. J. Int.*, *193*(3), 1537–1555. https://doi.org/10.1093/gji/ggt042

Kaneshima, Satoshi, & Matsuzawa, T. (2015). Stratification of earth's outermost core inferred from SmKS array data. *Progress in Earth and Planetary Science*, *2*(1). https://doi.org/10.1186/s40645-015-0046-5

Kawai, K., Takeuchi, N., & Geller, R. J. (2006). Complete synthetic seismograms up to 2 Hz for transversely isotropic spherically symmetric media. *Geophys. J. Int.*, *164*(2), 411–424. https://doi.org/10.1111/j.1365-246X.2005.02829.x

Kennett, B. L. N. (2021). Radial earth models revisited. *Geophysical Journal International*, *222*(3), 2189–2204. https://doi.org/10.1093/GJI/GGAA298

Kennett, B. L. N., & Engdahl, E. R. (1991). Traveltimes for global earthquake location and phase

identification. *Geophys. J. Int.*, *105*(2), 429–465. https://doi.org/10.1111/j.1365-246X.1991.tb06724.x

Kennett, B. L. N., & Gudmundsson, O. (1996). Ellipticity corrections for seismic phases. *Geophys. J. Int.*, *127*(1), 40–48. https://doi.org/10.1111/j.1365-246X.1996.tb01533.x

Kennett, B. L. N., Engdahl, E. R., & Buland, R. (1995). Constraints on seismic velocities in the Earth from traveltimes. *Geophys. J. Int.*, *122*, 108–124. https://doi.org/10.1111/j.1365-246X.1995.tb03540.x

Komatitsch, D., & Tromp, J. (2002a). Spectral-element simulations of global seismic wave propagation—I. Validation, *Geophysical Journal International*, *149*(2), 390–412. https://doi.org/10.1046/j.1365-246X.2002.01653.x

Komatitsch, D., & Tromp, J. (2002b). Spectral-element simulations of global seismic wave propagation - II. Three-dimensional models, oceans, rotation and self-gravitation. *Geophysical Journal International*, *150*(1), 303–318. https://doi.org/10.1046/j.1365-246X.2002.01716.x

Komatitsch, D, Xie, Z., Bozdağ, E., Sales de Andrade, E., Peter, D., Liu, Q. & Tromp, J., 2016. Anelastic sensitivity kernels with parsimonious storage for adjoint tomography and full waveform inversion, *Geophys. J. Int.*, doi: 10.1093/gji/ggw224.

Komatitsch, D., Barnes, C., & Tromp, J. (2002). Wave propagation near a fluid-solid interface: A spectral-element approach. *Geophysics*, *65*(2), 623–631. https://doi.org/10.1190/1.1444758

Kustowski, B., Ekström, G., & Dziewoński, A. M. (2008). The shear-wave velocity structure in the upper mantle beneath Eurasia. *Geophys. J. Int.*, *174*, 978–992. https://doi.org/10.1111/j.1365-246X.2008.03865.x

Liu Q. and Tromp, J., 2008. Finite-frequency Sensitivity Kernels for Global Seismic Wave Propagation based upon Adjoint Methods, *Geophysical Journal International*, 174(1), 265-286.

Long, M. D., & Lynner, C. (2015). Seismic anisotropy in the lowermost mantle near the Perm Anomaly. *Geophys. Res. Lett.*, *42*(17), 7073–7080. https://doi.org/10.1002/2015GL065506

Long, M. D., Jackson, K. G., & McNamara, J. F. (2016). SKS splitting beneath Transportable Array stations in eastern North America and the signature of past lithospheric deformation. *Geochem. Geophys. Geosyst.*, *17*(1), 2–15. https://doi.org/10.1002/2015GC006088

Lynner, C., & Long, M. D. (2014). Lowermost mantle anisotropy and deformation along the boundary of the African LLSVP. *Geophys. Res. Lett.*, *41*(10), 3447–3454. https://doi.org/10.1002/2014GL059875

Ma, X., & Tkalčić, H. (2023). CCMOC: A new view of the Earth's outer core through the global coda correlation wavefield. *Physics of the Earth and Planetary Interiors*, *334*(October 2022). https://doi.org/10.1016/j.pepi.2022.106957

Martha Savage. (1999). Seismic anisotropy and mantle deformation: What have we learned from shear wave splitting? *Reviews of Geophysics*, (98), 65–106. https://doi.org/10.1029/98RG02075

Morelli, A., & Dziewonski, M. (1993). Body wave traveltimes and a spherically symmetric P- and S-wave velocity model. *Geophys. J. Int.*, *112*, 178–194.

Marquering, H., Dahlen, F. A., Nolet, G., 1999. Three-dimensional sensitivity kernels for finite-frequency traveltimes: the banana-doughnut paradox, *Geophysical Journal International*, 137(3), 805–815, https://doi.org/10.1046/j.1365-246x.1999.00837.x.

Mound, J., Davies, C., Rost, S., & Aurnou, J. (2019). Regional stratification at the top of Earth's

core due to core–mantle boundary heat flux variations. *Nature Geoscience*, *12*(July). https://doi.org/10.1038/s41561-019-0381-z

Niu, F., & Perez, A. M. (2004). Seismic anisotropy in the lower mantle: A comparison of waveform splitting of SKS and SKKS. *Geophysical Research Letters*, *31*(24), 1–4. https://doi.org/10.1029/2004GL021196

Randall, M. J. (1971). A Revised Travel-Time Table for S. *Geophysical Journal of the Royal Astronomical Society*, *22*(3), 229–234. https://doi.org/10.1111/j.1365-246X.1971.tb03595.x

Ritsema, J., Ni, S., Helmberger, D. V, & Crotwell, H. P. (1998). Anomalous shear velocity reductions and gradients in the lower mantle beneath Africa. *Geophys. Res. Lett.*, *25*(23), 4245–4248.

Ritsema, J., Deuss, A., Van Heijst, H. J., & Woodhouse, J. H. (2011). S40RTS: A degree-40 shear-velocity model for the mantle from new Rayleigh wave dispersion, teleseismic traveltime and normal-mode splitting function measurements. *Geophys. J. Int.*, *184*(3), 1223–1236. https://doi.org/10.1111/j.1365-246X.2010.04884.x

Rost, S., & Thomas, C. (2002). Array seismology: Methods and applications. *Reviews of Geophysics*, *40*(3). https://doi.org/10.1029/2000RG000100

Selby, N. D. (2008). Application of a generalized F detector at a seismometer array. *Bull. Seism. Soc. Am.*, *98*(5), 2469–2481. https://doi.org/10.1785/0120070282

Silver, P. G., & Savage, M. K. (1994). The Interpretation of Shear-Wave Splitting Parameters In the Presence of Two Anisotropic Layers. *Geophysical Journal International*, *119*(3), 949–963. https://doi.org/10.1111/j.1365-246X.1994.tb04027.x

Souriau, A., & Poupinet, G. (1991). A study of the outermost liquid core using differential travel times of the SKS, SKKS and S3KS phases. *Physics of the Earth and Planetary Interiors*,

*68*(1–2), 183–199. https://doi.org/10.1016/0031-9201(91)90017-C

Stevenson, D. J. (1987). Limits on lateral density and velocity variations in the Earth's outer core. *Geophys. J. R. Astr. Soc.*, *88*(1), 311–319. https://doi.org/10.1111/j.1365-246X.1987.tb01383.x

Tanaka, S. (2004). Seismic detectability of anomalous structure at the top of the Earth's outer core with broadband array analysis of SmKS phases. *Phys. Earth Planet. Int.*, *141*(3), 141–152. https://doi.org/10.1016/j.pepi.2003.11.006

Tanaka, S. (2007). Possibility of a low P-wave velocity layer in the outermost core from global SmKS waveforms. *Earth Planet. Sci. Lett.*, *259*, 486–499. https://doi.org/10.1016/j.epsl.2007.05.007

Tanaka, S. (2014). Broadband waveform modeling with the spectral element method on Earth Simulator for the study of the structure at the top of the Earth's outer core. *JAMSTEC Report of Research and Development*, *19*(0), 1–9. https://doi.org/10.5918/jamstecr.19.1

Tang, V., Zhao, L., & Hung, S. H. (2015). Seismological evidence for a non-monotonic velocity gradient in the topmost outer core. *Scientific Reports*, *5*, 1–5. https://doi.org/10.1038/srep08613

Tromp, J., Tape, C. and Liu, Q., 2005. Seismic Tomography, Adjoint Methods, Time Reversal, and Banana-Doughnut Kernels, *Geophysical Journal International*, 160(1), 195-216.

Van Tent, R., Deuss, A., Kaneshima, S., & Thomas, C. (2020). The signal of outermost-core stratification in body-wave and normal-mode data. *Geophysical Journal International*, *223*(2), 1338–1354. https://doi.org/10.1093/gji/ggaa368

Tesoniero, A., Leng, K., Long, M. D., & Nissen-Meyer, T. (2021). Full wave sensitivity of SK(K)S phases to arbitrary anisotropy in the upper and lower mantle. *Geophysical Journal*

*International*, *222*(1), 412–435. https://doi.org/10.1093/GJI/GGAA171

Tkalčić, H., Romanowicz, B., & Houy, N. (2002). Constraints on D″ structure using PKP (AB–DF), PKP (BC–DF) and PcP–P traveltime data from broad-band records. *Geophys. J. Int.*, *148*, 599–616. https://doi.org/10.1046/j.1365-246X.2002.01603.x

To, A., Romanowicz, B., Capdeville, Y., & Takeuchi, N. (2005). 3D effects of sharp boundaries at the borders of the African and Pacific Superplumes: Observation and modeling. *Earth Planet. Sci. Lett.*, *233*(1–2), 137–153. https://doi.org/10.1016/j.epsl.2005.01.037

Ventosa, S., & Romanowicz, B. (2015). Extraction of weak PcP phases using the slant-stacklet transform – II: constraints on lateral variations of structure near the core–mantle boundary. *Geophys. J. Int.*, *203*, 1227–1245. https://doi.org/10.1093/gji/ggv364

Vidale, J. E. (1987). Waveform effects of a high-velocity, subducted slab. *Geophys. Res. Lett.*, *14*(5), 542–545. https://doi.org/10.1029/GL014i005p00542

Wang, L., & Niu, F. (2019). Anomalous SmKS induced by postcritical reflection and refraction at the core-mantle boundary. *Science Bulletin*, *64*(21), 1601–1607. https://doi.org/10.1016/j.scib.2019.09.004

Ward, J., Nowacki, A., & Rost, S. (2020). Lateral Velocity Gradients in the African Lower Mantle Inferred From Slowness Space Observations of Multipathing. *Geochemistry, Geophysics, Geosystems*, *21*(8). https://doi.org/10.1029/2020GC009025

Whittaker, S., Thorne, M. S., Schmerr, N. C., & Miyagi, L. (2016). Seismic array constraints on the D″ discontinuity beneath Central America. *Journal of Geophysical Research: Solid Earth*, *121*(1), 152–169. https://doi.org/10.1002/2015JB012392

Wolf, J., & Long, M. D. (2022). Slab-driven flow at the base of the mantle beneath the northeastern Pacific Ocean. *Earth and Planetary Science Letters*, *594*, 117758.

https://doi.org/10.1016/j.epsl.2022.117758

Wolf, J., Frost, D. A., Long, M. D., Garnero, E., Aderoju, A. O., Creasy, N., & Bozdağ, E. (2023). Observations of Mantle Seismic Anisotropy Using Array Techniques: Shear-Wave Splitting of Beamformed SmKS Phases. *Journal of Geophysical Research: Solid Earth*, *128*(1). https://doi.org/10.1029/2022JB025556

Wu, W., & Irving, J. C. E. (2020). Array-Based Iterative Measurements of SmKS Travel Times and Their Constraints on Outermost Core Structure. *Journal of Geophysical Research: Solid Earth*, *125*(3), 1–17. https://doi.org/10.1029/2019JB018162

Young, C. J., & Lay, T. (1987). Evidence for a shear velocity discontinuity in the lower mantle beneath India and the Indian Ocean. *Phys. Earth Planet. Int.*, *49*(1–2), 37–53. https://doi.org/10.1016/0031-9201(87)90131-2

Yu, S., & Garnero, E. J. (2018). Ultralow Velocity Zone Locations: A Global Assessment. *Geochem. Geophys. Geosyst.*, *19*(2), 396–414. https://doi.org/10.1002/2017GC007281

Zhao, C., Garnero, E. J., Mcnamara, A. K., Schmerr, N., & Carlson, R. W. (2015). Seismic evidence for a chemically distinct thermochemical reservoir in Earth's deep mantle beneath Hawaii. *Earth Planet. Sci. Lett.*, *426*, 143–153. https://doi.org/10.1016/j.epsl.2015.06.012